

## Supplemental Information

### A hindered-urea vitrimer: recyclable for circular use and upcyclable for rechargeable battery

YanJun Wang, Yue Wang, Wenjing Duan, Xuang Bai, Pengyuan Liu, Chiwei Xu, Hongqin Wang, Jinjue Zeng, Qi Wang, Fanyu Zhou, Yuhang Meng, Lijun Yang, Chenghui Li, Zheng Hu, Xiangfen Jiang, Liang Jiang, Jingxin Lei, and Xuebin Wang

This file includes:

#### Supporting Figures

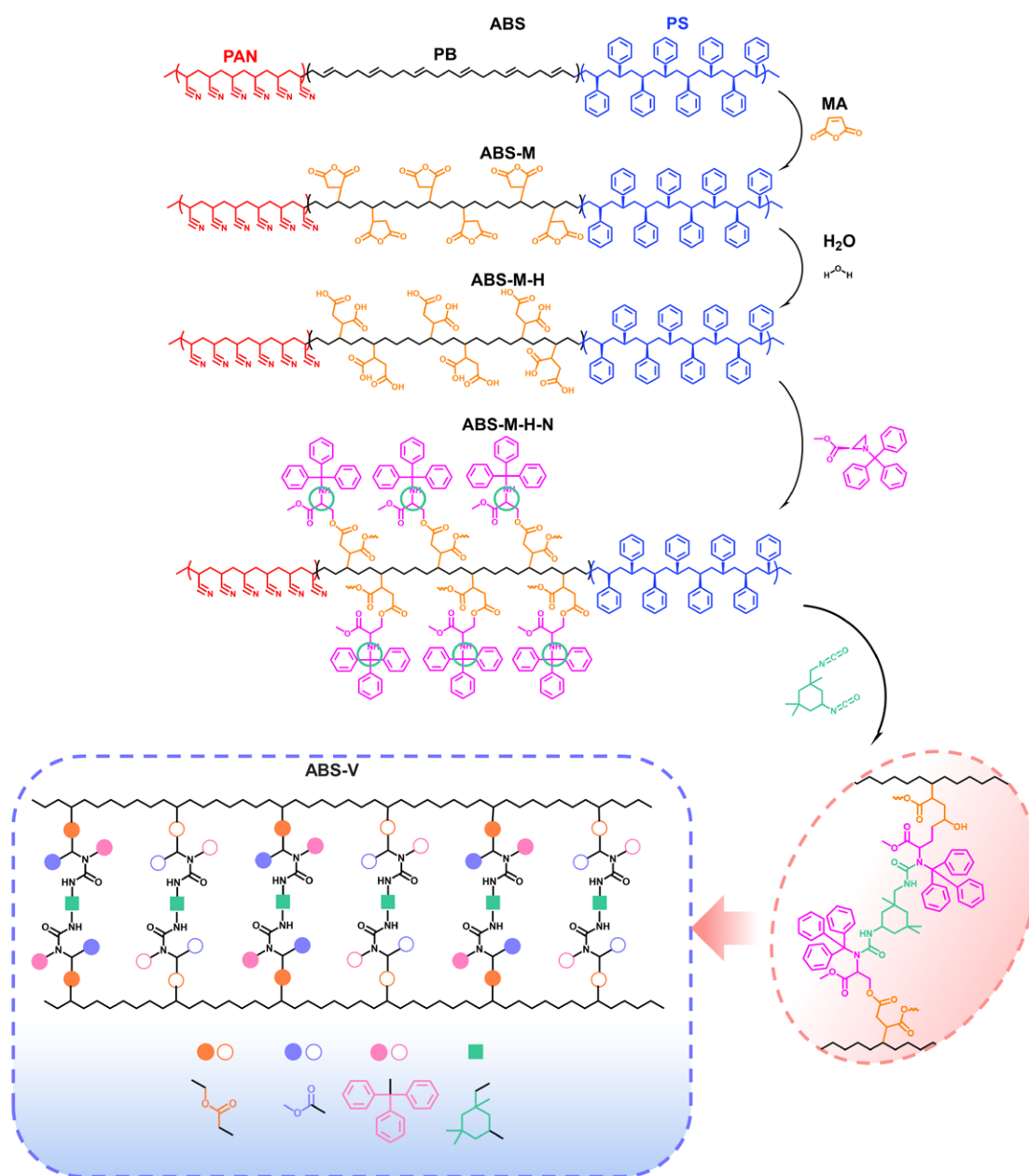
- Fig. S1. Synthesis procedure and chemical structure of ABS-V.
- Fig. S2. FTIR spectra of precursors and ABS-V.
- Fig. S3. Cross-linking characterizations of ABS-V.
- Fig. S4. Mechanical properties of ABS-V with different cross-linking degrees.
- Fig. S5. Thermal and thermo-mechanical tests of ABS-V.
- Fig. S6. Dynamic cross-linking tests of ABS-V.
- Fig. S7. Cross-linking characterizations of recycled ABS-V.
- Fig. S8. Self-healing performances of overlapped ABS-V.
- Fig. S9. Temperature-programmed synthesis for carbon from polymer.
- Fig. S10. Pore size distributions of ZnC-VP.
- Fig. S11. XPS spectra of ZnC-VP.
- Fig. S12. XPS spectra of ZnC-V.
- Fig. S13. XPS spectra of ZnC-A.
- Fig. S14. XPS spectra of C-A.
- Fig. S15. TG and DTG curves of heating polymer-and-ZnO mixture vs. polymer.
- Fig. S16. On-line TG-FTIR analysis of the volatile resultants during heating.
- Fig. S17. Reconstructed *in-situ* FTIR intensity of the volatile resultants following the programming temperature.
- Fig. S18. *Ex-situ* XRD patterns of residual solid intermediates during heating.
- Fig. S19. *Ex-situ* FTIR patterns of residual solid intermediates during heating.
- Fig. S20. Summary of pyrolysis processes.
- Fig. S21. Chemical evolution during synthesis of ZnC-V.

Fig. S22. CV curves at a scan speed of  $0.1 \text{ mV s}^{-1}$ .  
Fig. S23. GCD profiles at  $1 \text{ A g}^{-1}$ .  
Fig. S24. Tests of potassium ion storage kinetics of ZnC-VP.  
Fig. S25. Tests of potassium ion storage kinetics of ZnC-V.  
Fig. S26. Tests of potassium ion storage kinetics of ZnC-A.  
Fig. S27. Tests of potassium ion storage kinetics of C-A.  
Fig. S28. GCD profiles at different currents.  
Fig. S29. GCD profiles at  $5 \text{ A g}^{-1}$ .  
Fig. S30. Evaluations of Prussian Blue cathode.  
Fig. S31. Electrochemical behavior of ZnC-VP || Prussian Blue full cell.  
Fig. S32. Rate capability of full cell.  
Fig. S33. *Ex-situ* XRD patterns at marked discharge/charge potentials.  
Fig. S34. EIS Nyquist plots obtained with a bias of  $2.0 \text{ V vs K/K}^+$ .  
Fig. S35. EIS of ZnC-VP at different states during initial three cycles.  
Fig. S36. EIS of ZnC-V at different states during initial three cycles.  
Fig. S37. EIS of ZnC-A at different states during initial three cycles.  
Fig. S38. EIS of C-A at different states during initial three cycles.  
Fig. S39.  $R_{\text{SEI}}$  and  $R_{\text{ct}}$  under the initial three cycles.  
Fig. S40. GITT and chemical diffusion coefficients.  
Fig. S41. SEM images of ZnC-VP at different discharge and charge stages.  
Fig. S42. Elemental mappings of C, P, O, and K elements.

### **Supporting Tables**

Tab. S1. Survey of reported carbonaceous anode materials for PIBs.

## Supporting Figures



**Fig. S1.** Synthesis procedure and chemical structure of ABS-V.

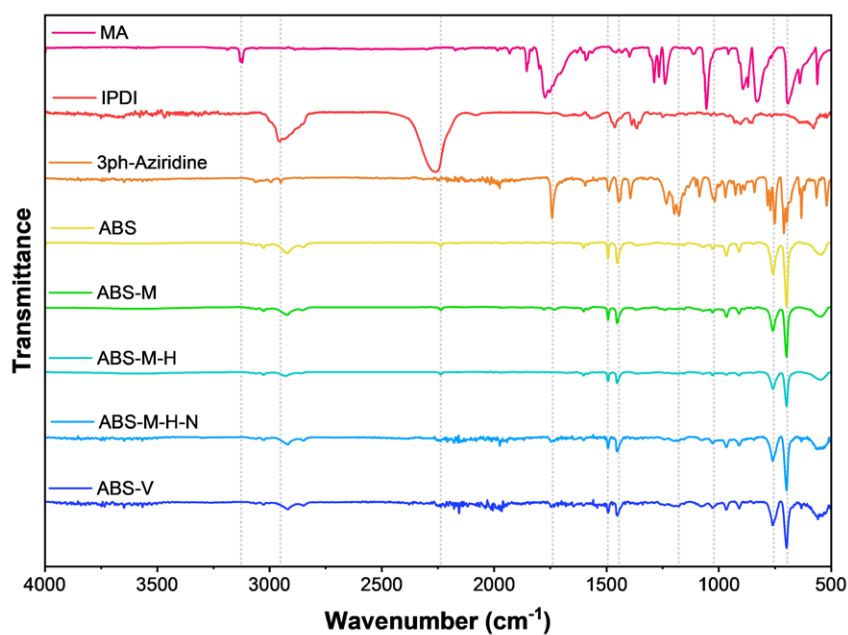


**Fig. S2.** FTIR spectra of precursors and cross-linked ABS-V.

Typical functional groups are identified as:

3400-3960  $\text{cm}^{-1}$  (O-H stretching of  $\text{H}_2\text{O}$ )

3064, 3026  $\text{cm}^{-1}$  (C-H stretching of benzene ring)

2922, 2849  $\text{cm}^{-1}$  (C-H stretching of  $-\text{CH}_2-$ )

2237  $\text{cm}^{-1}$  ( $\text{C}\equiv\text{N}$  stretching)

1748  $\text{cm}^{-1}$  ( $\text{C}=\text{O}$  stretching)

1602, 1494, 1453  $\text{cm}^{-1}$  (characteristic vibration of aromatic rings)

1076, 1028  $\text{cm}^{-1}$  (C-H in-plane bending of benzene ring)

966  $\text{cm}^{-1}$  (C-H out-of-plane bending of *trans*- $\text{RCH}=\text{CHR}$ )

760, 699  $\text{cm}^{-1}$  (C-H out-of-plane bending of benzene ring)

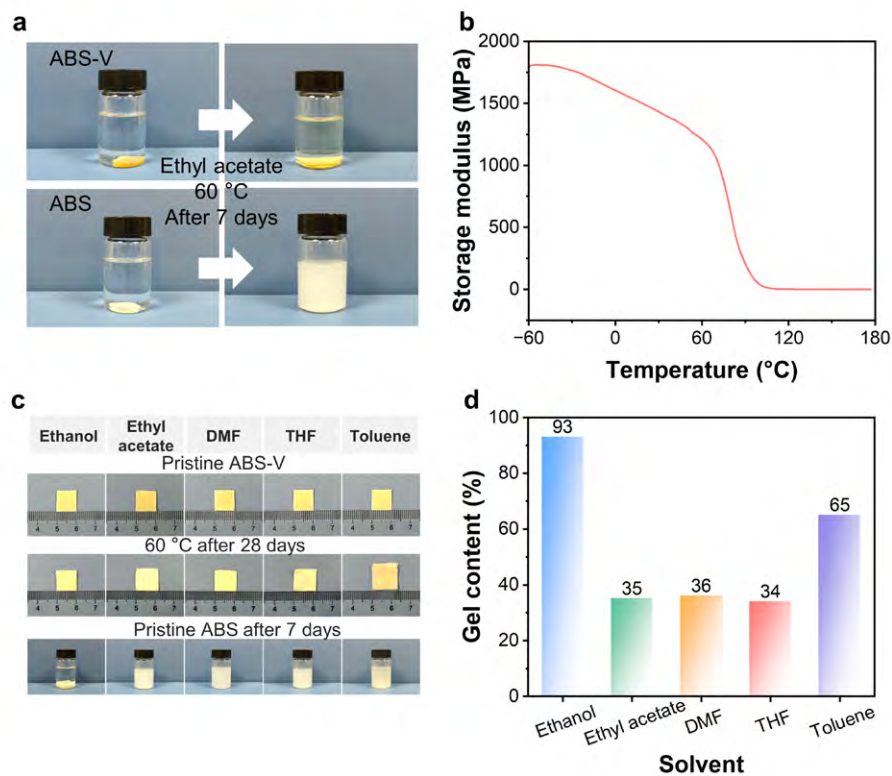


**Fig. S3.** Cross-linking characterizations of ABS-V. (a) Swelling of ABS-V and solubility of ABS in ethyl acetate at 60°C after 7 days. (b) Thermo-mechanical characterization of ABS-V. (c) Swelling of ABS-V in five solvents, including ethanol, ethyl acetate, DMF, THF, and toluene. (d) Gel content of ABS-V in five solvents with various polarity.

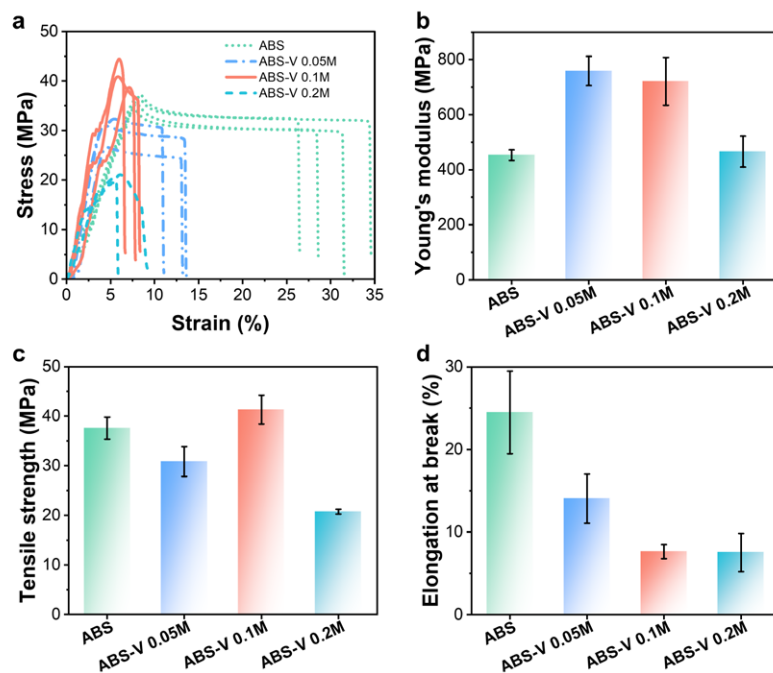


**Fig. S4.** Mechanical properties of ABS-V with different cross-linking degrees. (a) Stress-strain curves. (b) Young's modulus. (c) Tensile strength. (d) Elongation at break. The cross-linking degree increases from 0.05 M to 0.2 M.

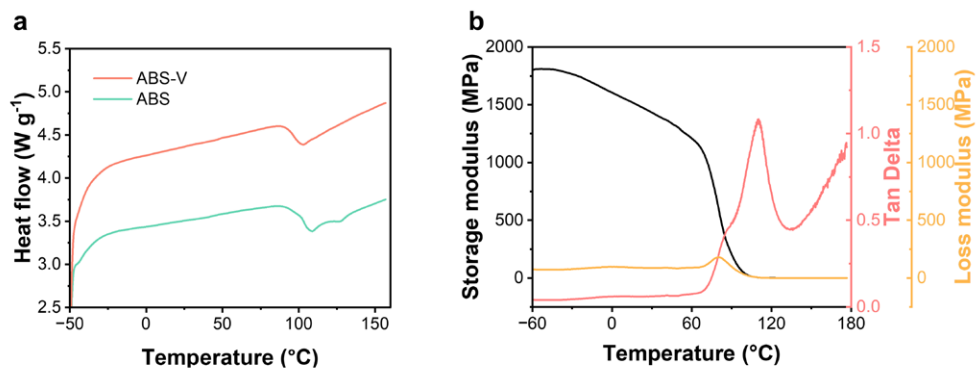


**Fig. S5.** Thermal and thermo-mechanical tests of ABS-V. (a) DSC curves. (b) DMA curves.

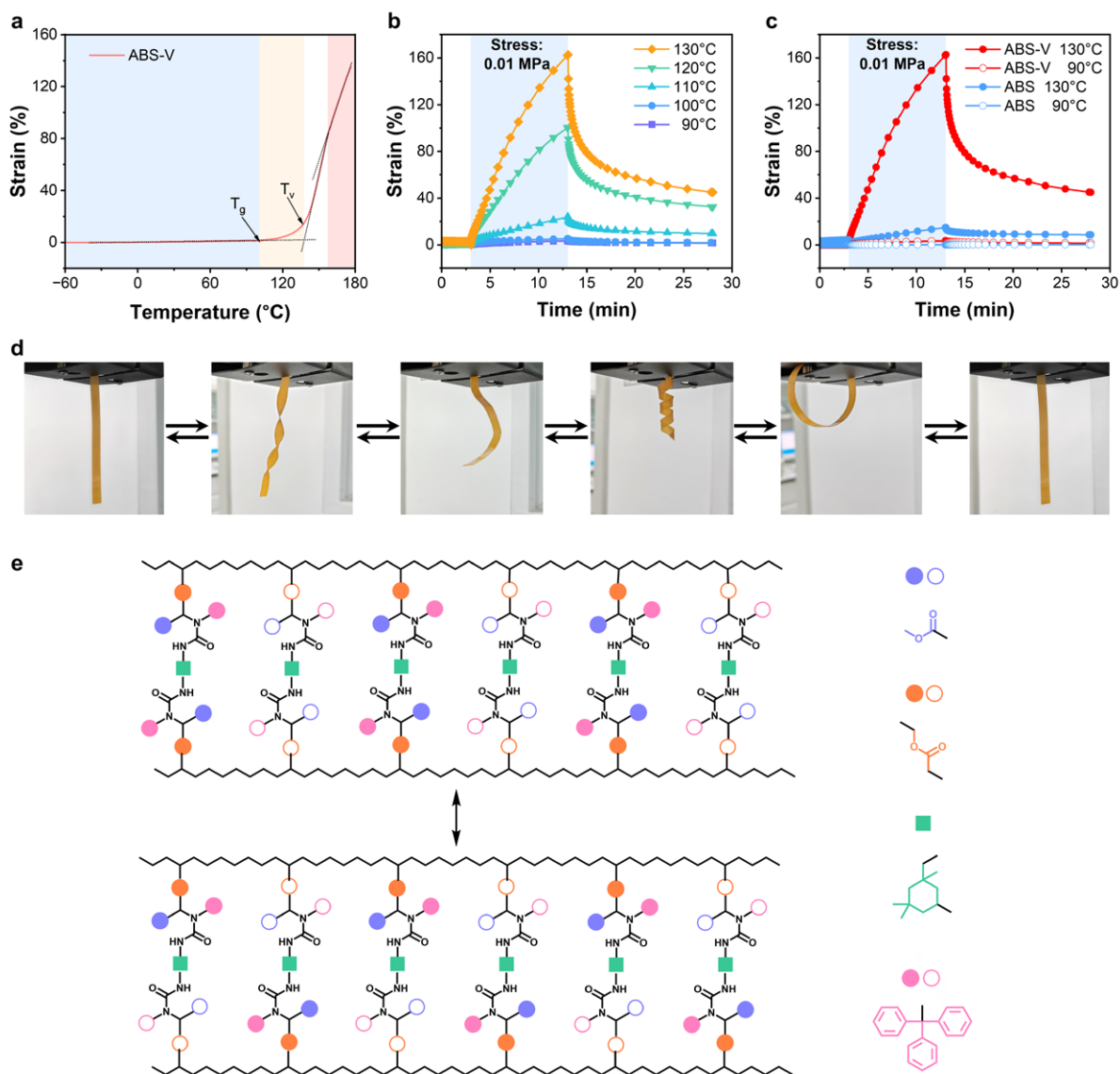


**Fig. S6.** Dynamic cross-linking tests of ABS-V. (a) Temperature dependence of thermal expansion. (b) Temperature-dependent creep behavior. (c) Creep behavior of ABS-V and ABS at 90°C and 130°C, respectively. The urea linkages strengthen the creep resistance of ABS-V at room temperature. At high temperatures, the  $\pi$ - $\pi$  interactions formed between the benzene rings in the cross-linked structure are weakened. At the same time, triphenylmethyl groups increase the spacing between molecular chains and reduce intermolecular forces, resulting in lower creep resistance of ABS-V at high temperatures compared to pristine ABS, which enhances processing performance. (d) Solid-state plasticity and permanent deformation of ABS-V at 120°C after 1 minute. (e) Schematic depiction of thermal-triggered reversible exchange mechanism of dynamic urea linkages.



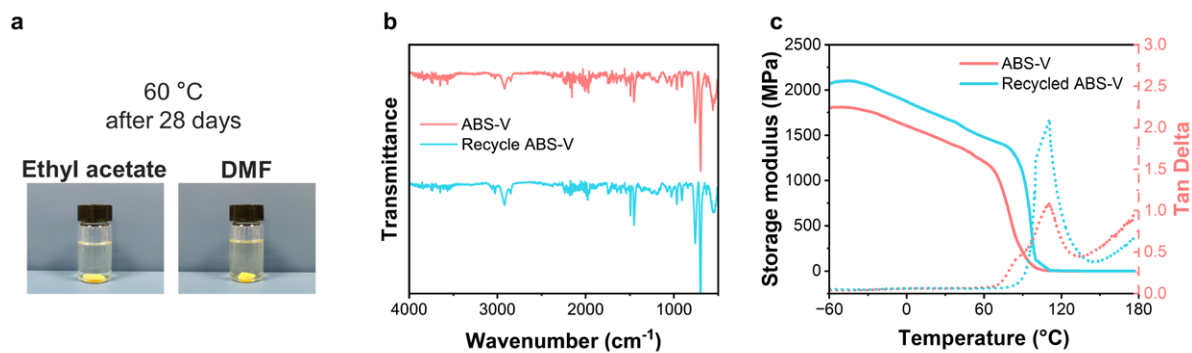


**Fig. S7.** Cross-linking character characterizations of recycled ABS-V. (a) Swelling of recycled ABS-V in ethyl acetate and DMF. (b) FTIR spectra of pristine and recycled ABS-V. (c) DMA curves.

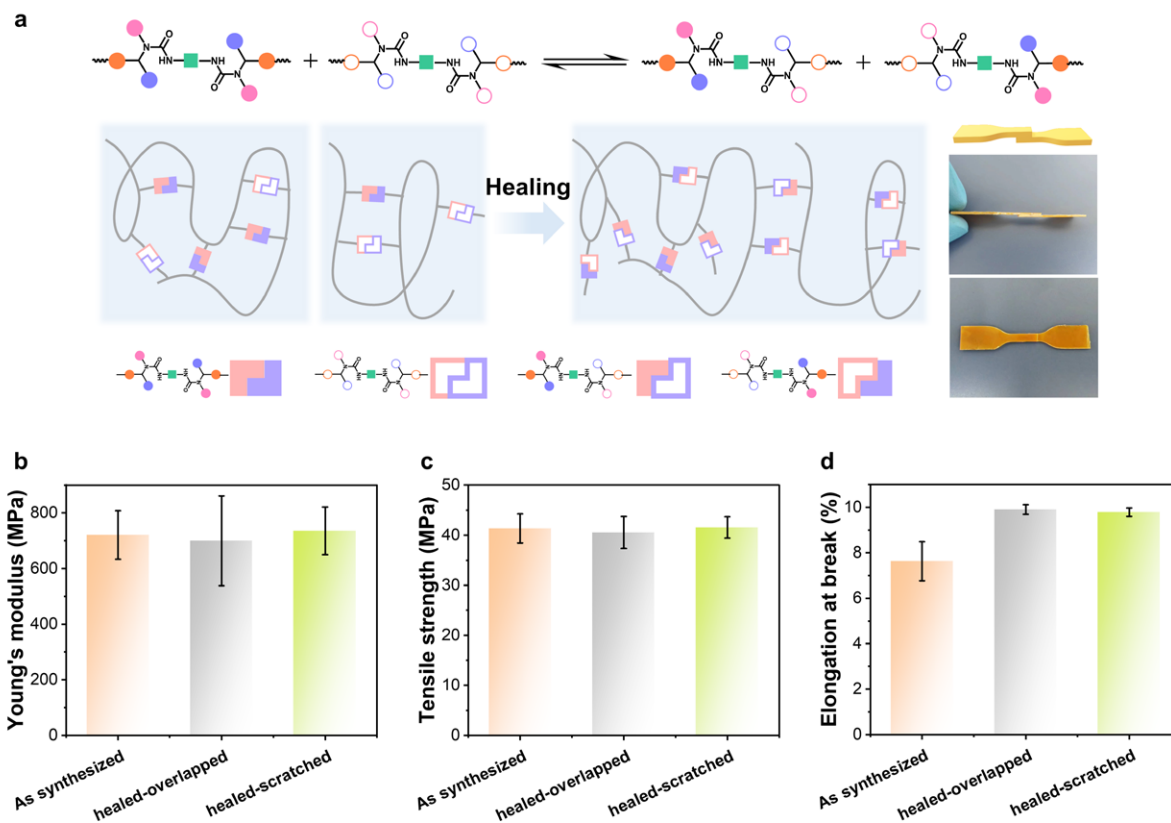


**Fig. S8.** Self-healing performances of overlapped ABS-V. (a) Schematic of thermal-triggered self-healing mechanism. (b-d) Young's modulus, tensile strength, and elongation at break of as synthesized and self-healed samples, respectively.

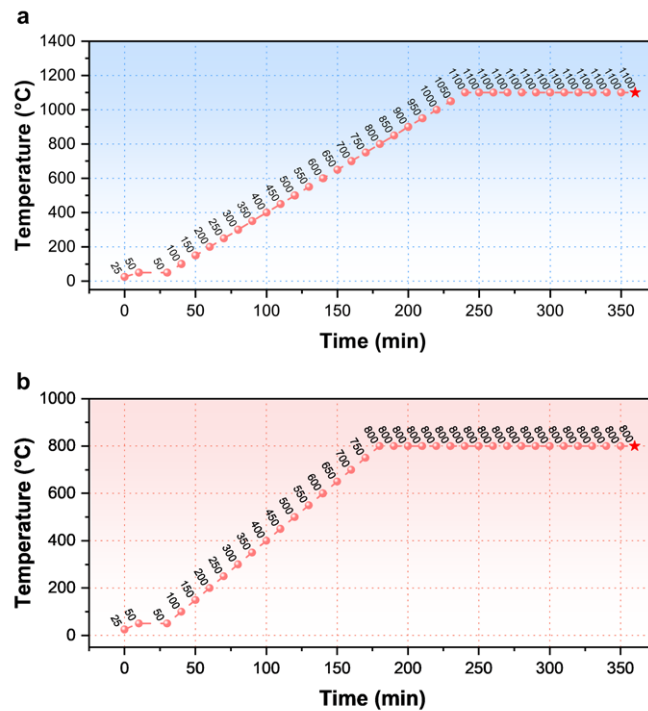


**Fig. S9.** Temperature-programmed synthesis for carbon from polymer. (a) Pyrolysis for producing ZnC-V, ZnC-A, and C-A, where the intermediate specimens were taken at the marked temperatures. (b) Pyrolysis for producing ZnC-VP.

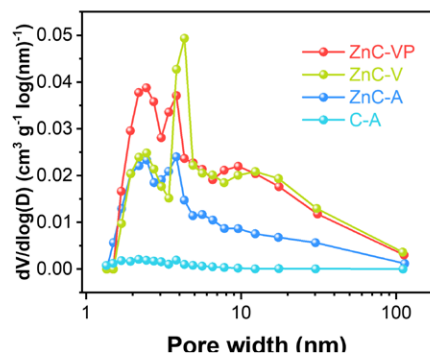


**Fig. S10.** Pore size distributions of ZnC-VP vs. others.

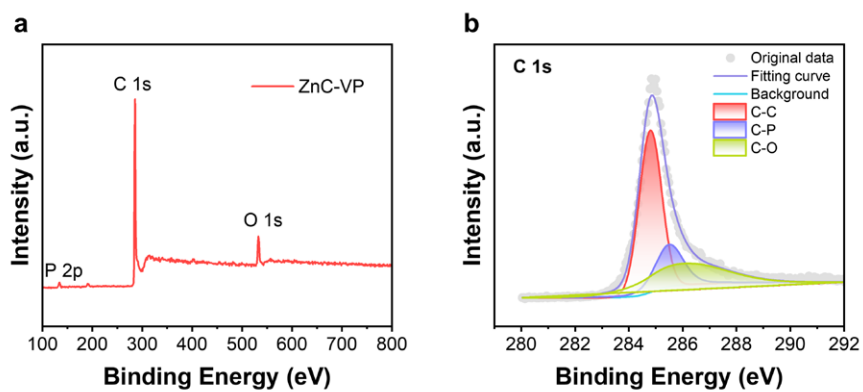


**Fig. S11.** XPS spectra of ZnC-VP. (a) Survey. (b) C 1s spectrum. C peak is fitted with three bonding forms of C-C (284.8 eV), C-P (285.5 eV), and C-O (286.3 eV).

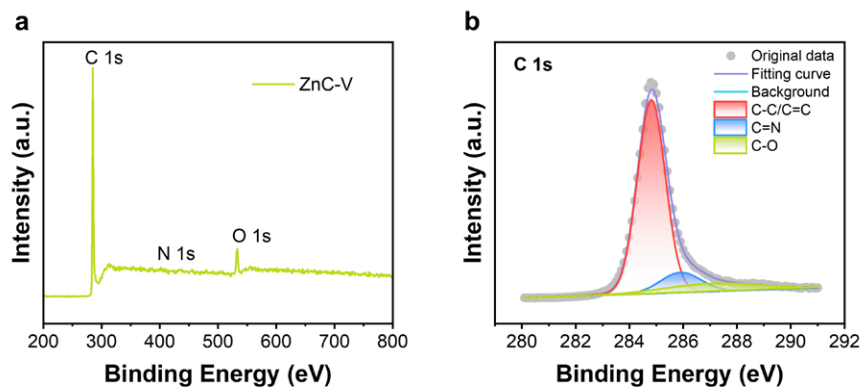


**Fig. S12.** XPS spectra of ZnC-V. (a) Survey. (b) C 1s spectrum.

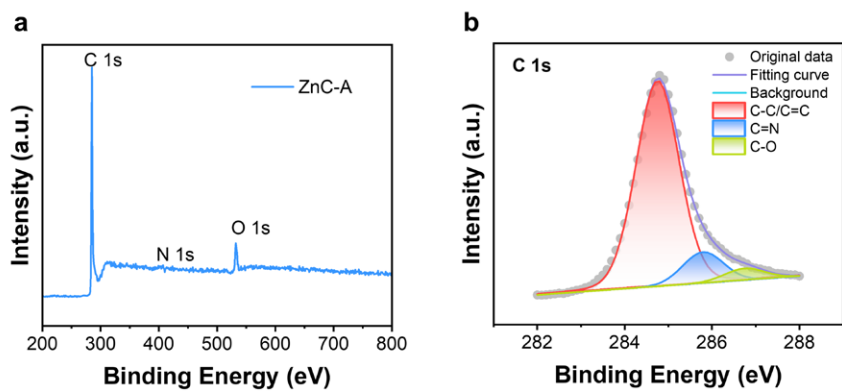


**Fig. S13.** XPS spectra of ZnC-A. (a) Survey. (b) C 1s spectrum.

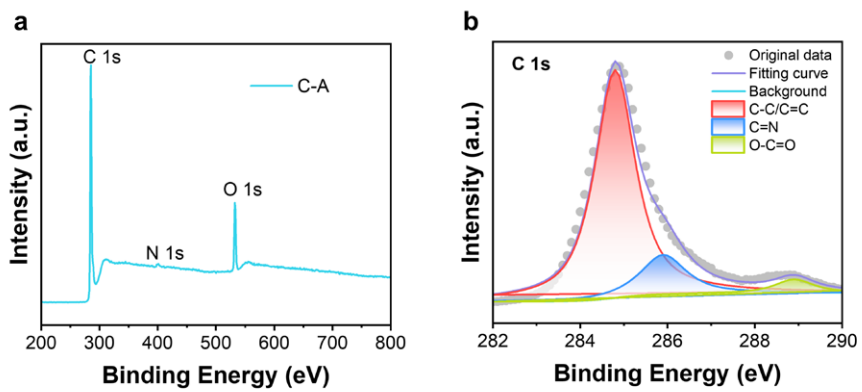


**Fig. S14.** XPS spectra of C-A. (a) Survey. (b) C 1s spectrum.



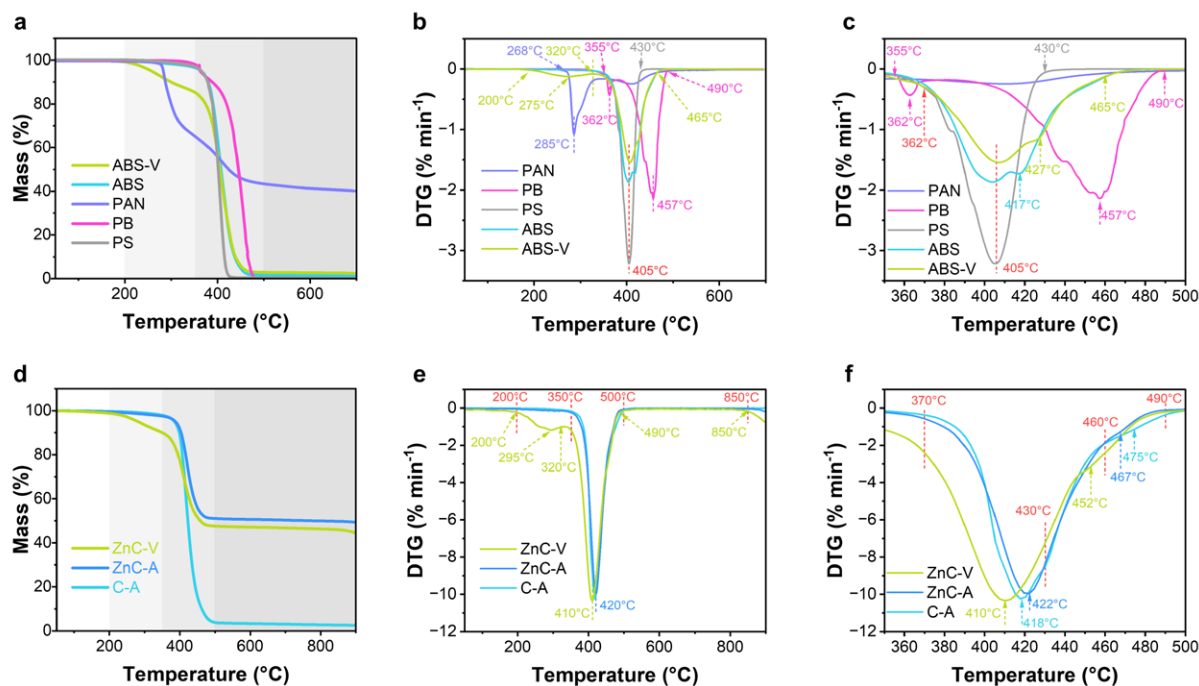


**Fig. S15.** TG and DTG curves of heating polymer-and-ZnO mixture vs. polymer. (a-c) TG and DTG curves of heating ABS-V, ABS, PAN, PB, and PS, respectively. (d-f) TG and DTG curves of heating ABS-V and ZnO, ABS and ZnO, and ABS for producing ZnC-V, ZnC-A, and C-A, respectively. Weight ratio for polymer-and-ZnO mixture is 1:1.

The details of TGA responses:

*i)* Below 200°C, slight mass loss was detected in either pure polymers or the mixture of polymer and ZnO. The mass losses of heating ABS-V, ABS, and PAN are 1.01%, 0.42% and 0.55%, which can be attributed to the volatilization of free water, residual DMF solvents, and unreacted monomer.

*ii)* At 200–350°C, the mass losses of heating ABS-V and the mixture account for 14.11% and 8.84%, respectively. The mass loss originates two aspects: *a)* decomposition of cross-linking linkages to release CO<sub>2</sub> (Fig. S17, from 205°C to 320°C), *b)* cyclization and dehydrogenation reaction in PAN units to release olefin (Fig. S17, beginning at 232°C), and decomposition reaction (beginning at 268°C) to release benzene derivative (Fig. S17, from 290°C to 370°C). The rapid mass loss of ABS-V and the mixture sustains until the ending of CO<sub>2</sub> release and cyclization reaction of PAN component at 320°C. In this stage, ABS, PB, and PS decompose slightly with a mass loss of only 2.92%, 1.4%, and 2.79%, respectively.

*iii)* At 350–500°C, all the polymers and mixtures undergo major decomposition and mass losses. The mass losses of ABS-V and ABS-V-and-ZnO mixture reach 81.99% and 42.42%, respectively. In this stage, the main mass loss originates from the decomposition of PB and PS blocks with mass losses of 98.52% and 96.53%, respectively. Pristine ABS exhibits a quicker

mass loss (95.01%) than that of ABS-V. The initial mass ratio of polymer to zinc oxide in the mixture is 1:1. Assuming that ZnO does not participate in the reaction at this stage, the mass losses of the mixtures should be half of the corresponding polymer, namely 41% for heating ABS-V and ZnO and 47.51% for heating ABS and ZnO. However, the real mass losses are 42.42% and 46.48%, suggesting a quicker mass loss speed for heating ABS-V and ZnO, as a result of ZnO-assisted accelerated pyrolysis for ZnC-V. ABS and ABS-V show two obvious mass loss stages: the first peaks in DTG curves at 405°C represent the decomposition of PS units, and the second peaks at 417–427°C imply the decomposition of major PB units and residual PAN units. The addition of ZnO improves the degradation temperature of polymers so that the maximum mass loss of first stage appears at 410°C and that of the second stage occurs at 452°C for ZnC-V. By contrast, the degradation of ABS in ABS and ZnO mixture is partial inhibited, which can be reflected by the slower mass loss and higher degradation temperature (the maximum mass loss at 422°C and 467°C, respectively). Compared to ABS and ZnO mixture, the lower decomposition temperature of PB and PS components in ABS-V and ZnO mixture may result in the quicker mass loss.

*iv*) At 500–850°C, the mass losses of PAN and ABS-V-and-ZnO mixture are 3.20% and 1.35%, respectively, and that of other pure polymers and the mixtures of polymers-and-ZnO are less than 0.5%. ABS resin (Aldrich Chemical Co.) containing 19–22% acrylonitrile, 37–39% butadiene, and 30–32% polystyrene units. Assuming that the pyrolysis of the three components in ABS does not affect each other, the theoretical carbon residue from pristine ABS pyrolysis should be *ca.* 8%. The real residue of 0.35% for pristine ABS demonstrates that the pyrolysis of three components is a complex process that affects each other.

*v*) Above 850°C, the mass loss originates the deep carbonization.

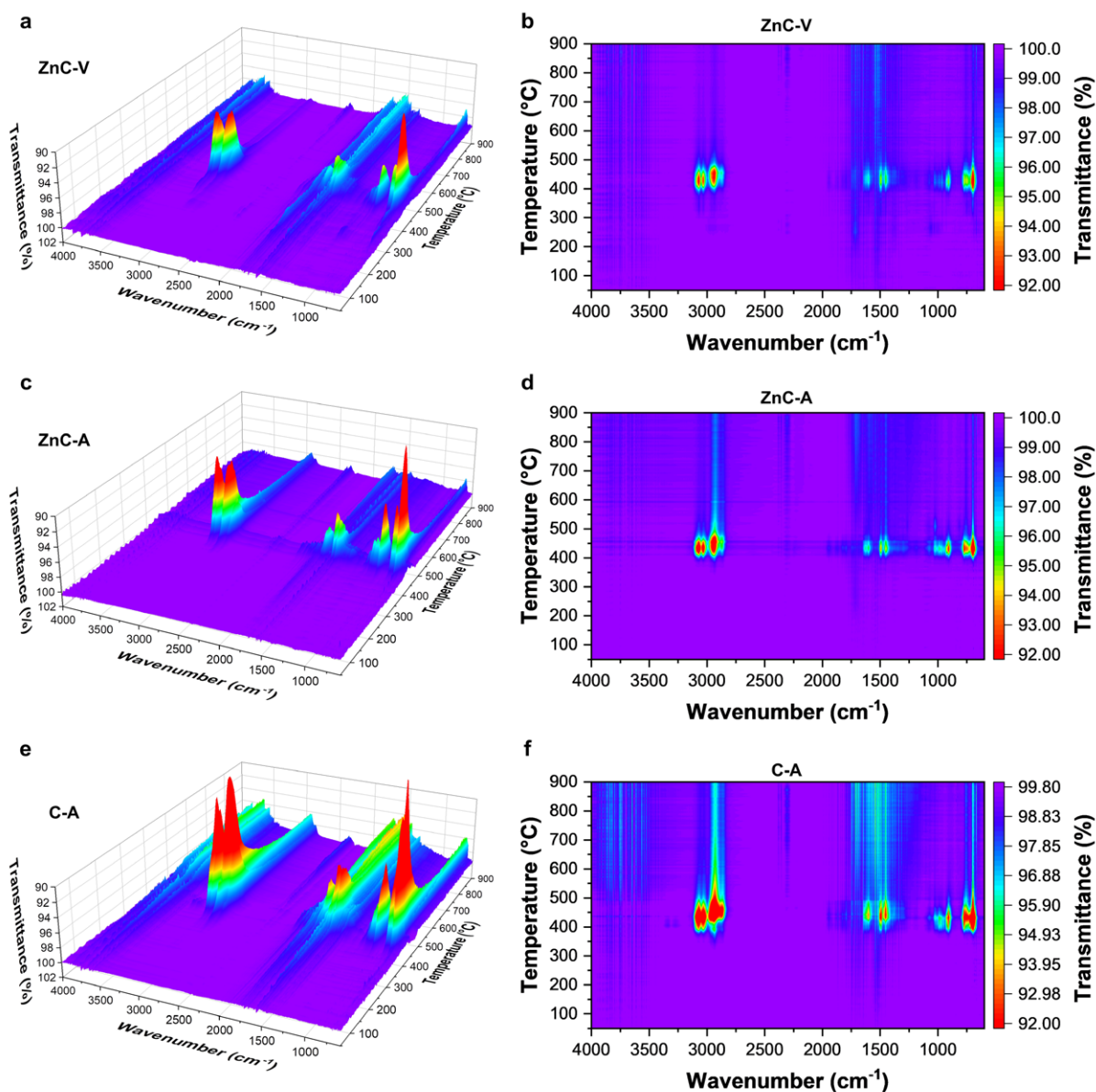


**Fig. S16.** On-line TG-FTIR analysis of the volatile resultants during heating. (a,b) Heating ABS-V and ZnO for producing ZnC-V. (c,d) Heating ABS and ZnO for producing ZnC-A. (e,f) Heating ABS for producing C-A. Weight ratio for polymer-and-ZnO mixture is 1:1.

Volatile resultants are identified as follows.

3512-4000  $\text{cm}^{-1}$  (O-H stretching of  $\text{H}_2\text{O}$ )

3070, 3029  $\text{cm}^{-1}$  (C-H stretching of benzene ring)

2936  $\text{cm}^{-1}$  (C-H stretching of  $-\text{CH}_2-$ )

2875  $\text{cm}^{-1}$  (C-H stretching of  $-\text{CH}_3$ )

2307, 2357, 2385  $\text{cm}^{-1}$  (asymmetric stretching of  $\text{CO}_2$ )

2242  $\text{cm}^{-1}$  ( $\text{C}\equiv\text{N}$  stretching)

2179  $\text{cm}^{-1}$  ( $\text{C}\equiv\text{O}$  stretching of CO)

1829, 1747  $\text{cm}^{-1}$  (C=O stretching of carboxyl)

1715  $\text{cm}^{-1}$  (C=O stretching of ketonic carbonyl)  
1646  $\text{cm}^{-1}$  (C=C stretching)  
1607, 1496, 1456  $\text{cm}^{-1}$  (characteristic vibration of benzene rings)  
1302  $\text{cm}^{-1}$  (C-H bending in  $\text{CH}_4$ )  
1085, 1028  $\text{cm}^{-1}$  (C-H in-plane bending of benzene ring)  
965  $\text{cm}^{-1}$  (C-H out-of-plane bending of *trans*-RCH=CHR)  
990, 910  $\text{cm}^{-1}$  (C-H out-of-plane bending of RCH=CH<sub>2</sub>)  
949  $\text{cm}^{-1}$  (C-H bending in  $\text{C}_2\text{H}_4$ )  
928  $\text{cm}^{-1}$  (N-H bending of  $\text{NH}_3$ )  
772, 695  $\text{cm}^{-1}$  (C-H out-of-plane bending of monosubstituted benzene ring)

According to the aforementioned analysis, the compounds from ABS degradation can be classified into four categories.<sup>1-6</sup>

i) Hydrocarbons in gases, including methane, ethylene, ethane, propylene, propane, unsaturated and saturated  $\text{C}_4$  and  $\text{C}_5$  hydrocarbons, benzene, toluene, ethylbenzene, and styrene;

ii) Hydrocarbons in oil, including butylene, cyclohexane, benzene, toluene, ethylbenzene, styrene, isopropylbenzene,  $\alpha$ -methylstyrene, 1,3-diphenylpropane;

iii) N-containing compounds, including ammonia, hydrogen cyanide, acetonitrile, acrylonitrile, propionitrile, metacrylonitrile, isobutyronitrile, crotonitrile, phenylacetonitrile, 2-phenylpropylonitrile, 4-phenylbutyronitrile, methylquinoline or  $\alpha$ -naphthylamine, dimethylquinoline isomers, *N*-benzylpyrrole, phenylethylamine, *N*-benzylaniline, hexadecanonitrile, octadecanonitrile, and so on;

iv) CO and  $\text{CO}_2$ .

Based on the identified characteristic peaks, the *in-situ* FTIR intensity of ten volatile resultants is reconstructed in Fig. S17. The adopted characteristic peaks are as follows:  $\text{H}_2\text{O}$  at 3839  $\text{cm}^{-1}$ ,  $\text{NH}_3$  at 928  $\text{cm}^{-1}$ , CO at 2179  $\text{cm}^{-1}$ ,  $\text{CO}_2$  at 2307  $\text{cm}^{-1}$ , cyano-containing compounds at 2242  $\text{cm}^{-1}$ , benzene derivatives at 3070  $\text{cm}^{-1}$ , alkanes at 2936  $\text{cm}^{-1}$ , olefins at 965  $\text{cm}^{-1}$ ,  $\text{CH}_4$  at 1302  $\text{cm}^{-1}$ , and  $\text{C}_2\text{H}_4$  at 949  $\text{cm}^{-1}$ .

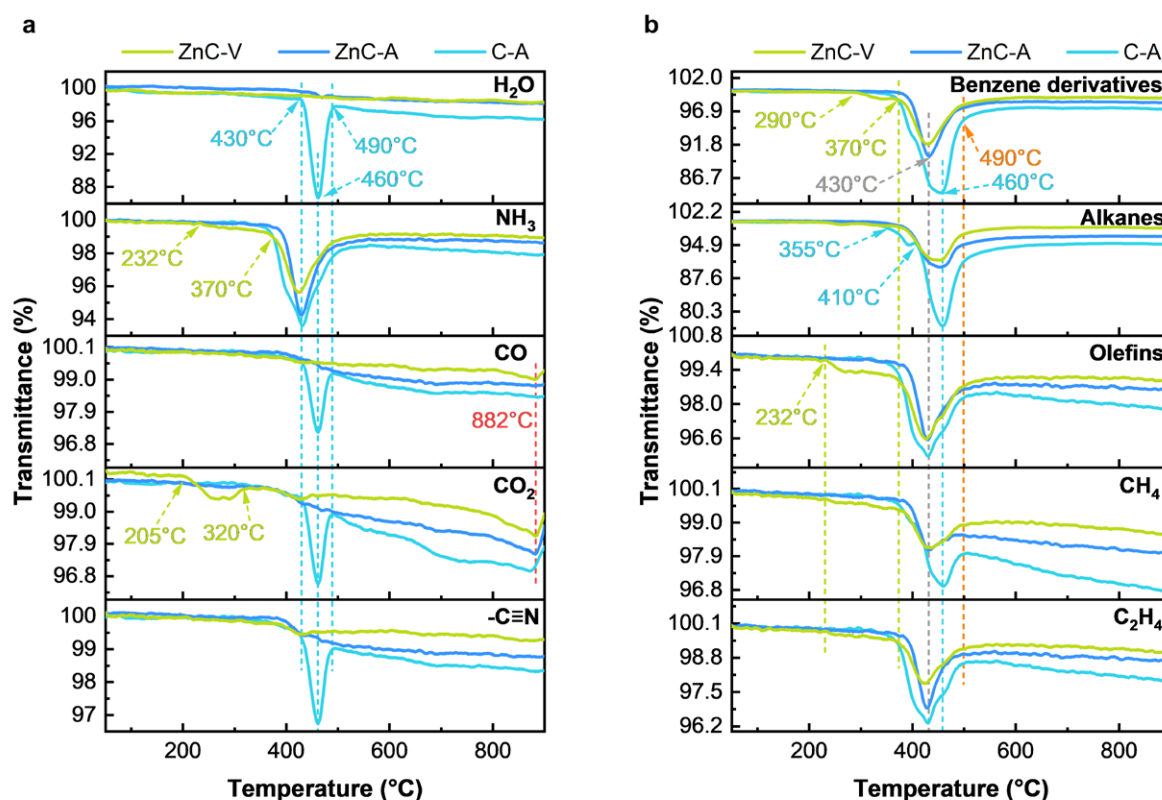


**Fig. S17.** Reconstructed *in-situ* FTIR intensity of the volatile resultants following the programming temperature. (a) Signals of H<sub>2</sub>O, NH<sub>3</sub>, CO, CO<sub>2</sub>, and cyano-containing compounds. (b) Signals of benzene derivatives, alkanes, olefins, CH<sub>4</sub>, and C<sub>2</sub>H<sub>4</sub>.

The details of *in-situ* FTIR responses of volatile resultants are as follows.

- i) At 50–200°C, no obvious volatile products were detected.
- ii) At 200–320°C, a lower intensity of CO<sub>2</sub> signal of ZnC-V sample implies the decomposition of cross-linking linkages (maybe ester and urea bonds) to release CO<sub>2</sub>.
- iii) At 232–370°C, a decreased intensity of NH<sub>3</sub>, olefin, CH<sub>4</sub>, and C<sub>2</sub>H<sub>4</sub> signals of ZnC-V may stem from the cyclization and dehydrogenation reaction in cross-linking linkage units.
- iv) At 290°C, a decreased intensity of benzene derivative of ZnC-V indicates the elimination of benzene-containing groups in cross-linking linkage units.
- v) At 355–410°C, a decreased intensity of alkane signal of ZnC-A corresponds with the first decomposition stage of PB in DTG curves. The absence of alkane signal of ZnC-V in this stage proves that cross-linking linkages improve the thermal stability of PB units in ABS.
- vi) At 370–490°C, the rapid decreased intensity in multi-signals of three samples proves a complex chemical process. At 370–430°C, the signals of NH<sub>3</sub>, benzene derivatives, alkanes, olefins, CH<sub>4</sub>, and C<sub>2</sub>H<sub>4</sub> in all three samples show rapid reduction, suggesting the decomposition of PS units according to DTG curves of polymers. The maximum signals at 430°C imply the

accompanying decomposition of PAN and PB units. At 430–490°C, the increased intensity signals of these products disclose the gradual elimination of PAN and PB units. However, at 430–490°C, sharp signals of H<sub>2</sub>O, CO, CO<sub>2</sub>, and cyano-containing compounds only appear in C-A instead of ZnC-A and ZnC-V, suggesting that these volatile products participate in the reaction with ZnO. The relatively gentle decline curve of these signals in ZnC-V indicates that more decomposition is involved in the reaction with ZnO.

*vii)* At 490–900°C, the gradually decreased signals of cyano-containing compounds, olefins, CH<sub>4</sub>, and C<sub>2</sub>H<sub>4</sub> in all three samples indicating the further decomposition of solid residues. The obvious inflection points at 882°C especially in ZnC-V indicates the elimination of oxygen-containing functional groups.

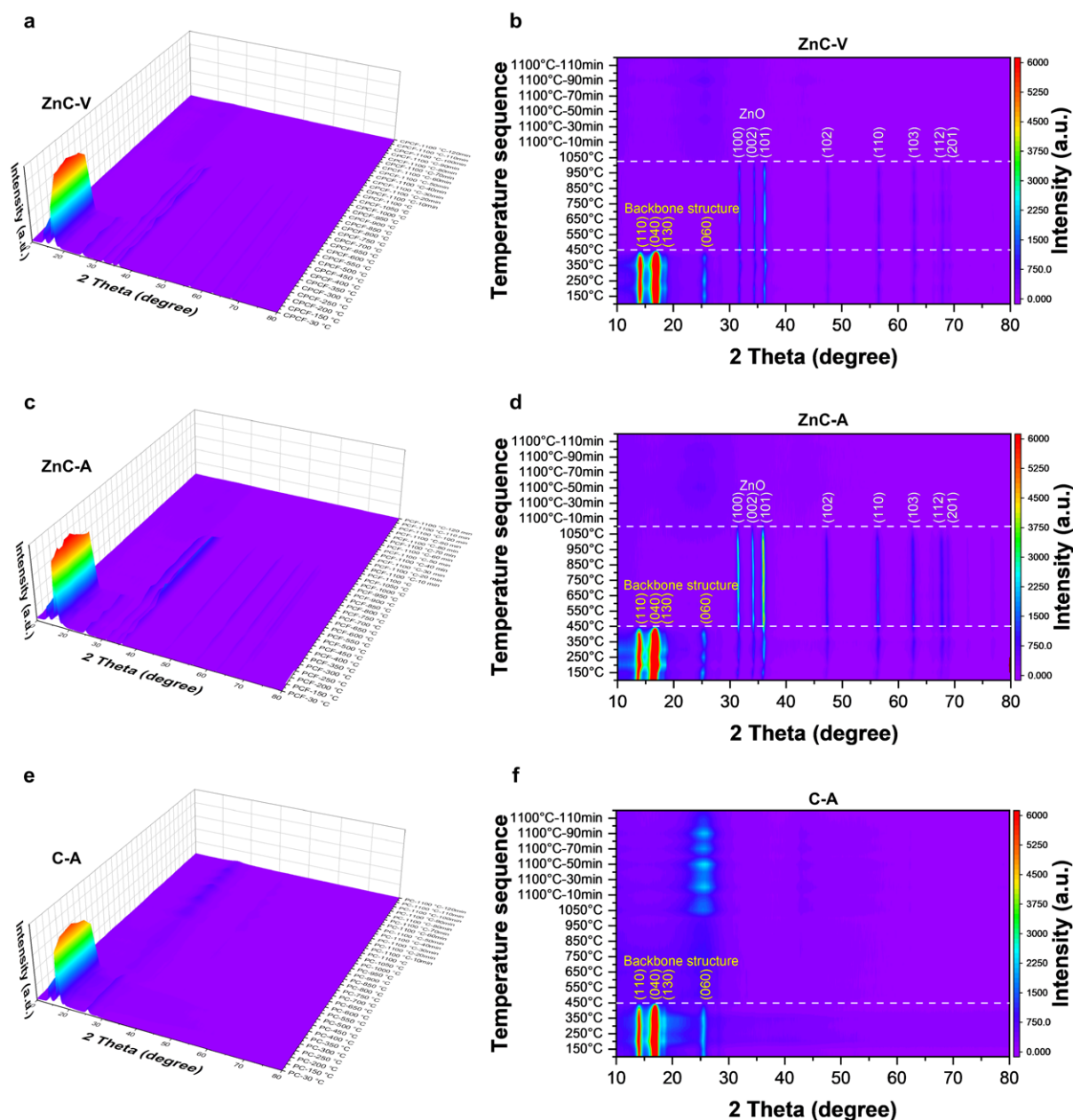


**Fig. S18.** *Ex-situ* XRD patterns of residual solid intermediates during heating. (a,b) ZnC-V precursor. (c,d) ZnC-A precursor. (e,f) C-A precursor. Weight ratio for polymer-and-ZnO mixture is 5:9.

The details of *ex-situ* XRD responses of residual solid intermediates are as follows.

i) At 50–450°C, the peaks at 14.01°, 16.87°, 18.52°, and 25.34° correspond to (110), (040), (130), and (060) crystalline planes of polypropylene (PP) resin, respectively. The structure of PP is similar to the backbone structure of ABS. Therefore, the signal of PP structure can demonstrate the existence of backbone structure of ABS. The backbone structure of ABS has basically completely polycondensated at 450°C.

*ii*) At 50–1100°C, the peaks at 31.76°, 34.41°, 36.22°, 47.50°, 56.57°, 62.94°, 67.95°, and 69.05° correspond to (100), (002), (101), (102), (110), (103), (112), and (201) crystalline planes of ZnO in ZnC-A or ZnC-V. The ZnO signal of ZnC-A sample disappears at 1100°C, but that of ZnC-V disappears at 1000°C. The lower temperature of ZnO signal disappearance demonstrates an earlier reaction between ABS-V and ZnO, which can be proved by the mass loss from 350°C to 500°C in TGA curves.

*iii*) At 50–1100°C, no signals of Zn or other Zn-containing compounds are observed in the residual solid intermediates. It suggests the complete volatilization of Zn.



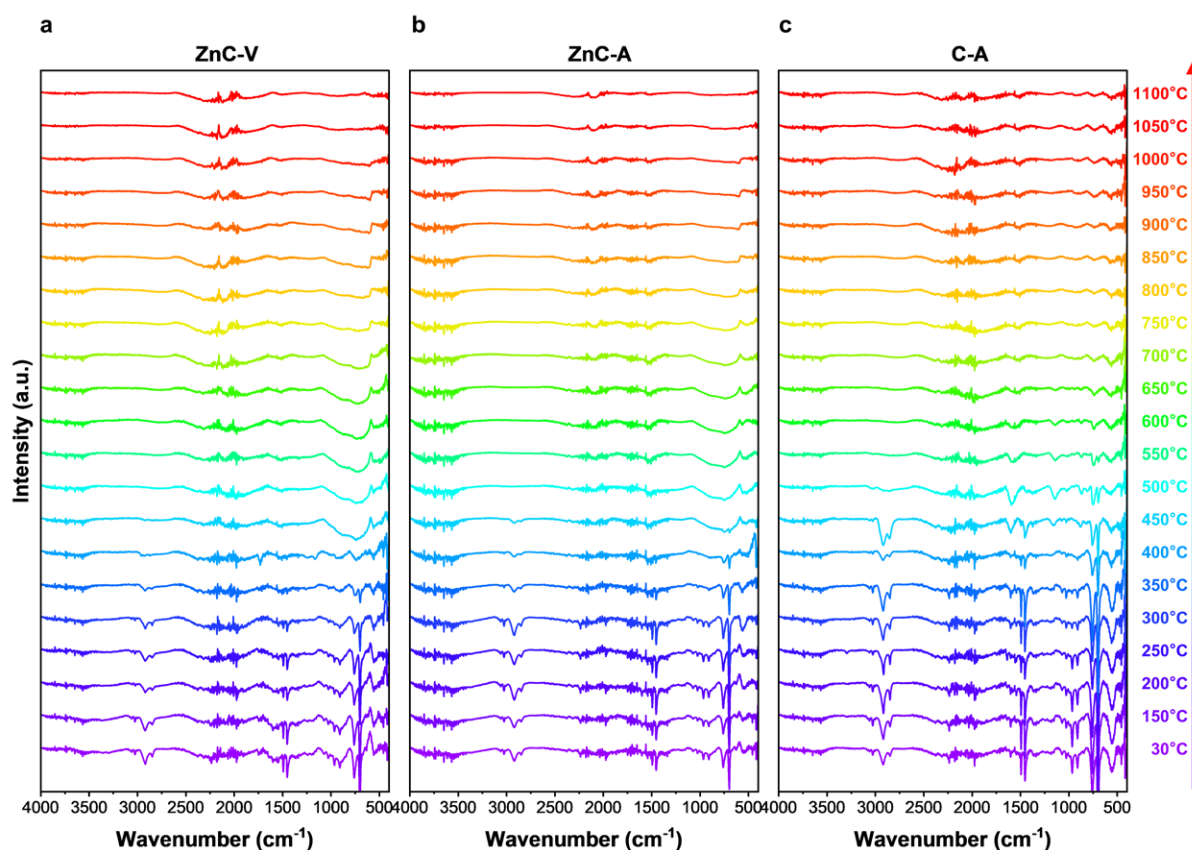


**Fig. S19.** *Ex-situ* FTIR patterns of residual solid intermediates during heating. (a) ZnC-V precursor. (b) ZnC-A precursor. (c) C-A precursor. Weight ratio for polymer-and-ZnO mixture is 5:9.

The residual solid intermediates are identified as follows.

3400-3960  $\text{cm}^{-1}$  (O-H stretching of  $\text{H}_2\text{O}$ )

3064, 3026  $\text{cm}^{-1}$  (C-H stretching of benzene ring)

2922, 2849  $\text{cm}^{-1}$  (C-H stretching of  $-\text{CH}_2-$ )

2378, 2313  $\text{cm}^{-1}$  (asymmetric stretching of  $\text{CO}_2$ )

2237  $\text{cm}^{-1}$  ( $\text{C}\equiv\text{N}$  stretching)

1748  $\text{cm}^{-1}$  ( $\text{C}=\text{O}$  stretching)

1639  $\text{cm}^{-1}$  ( $\text{C}=\text{C}$  stretching)

1602, 1494, 1453  $\text{cm}^{-1}$  (characteristic vibration of benzene rings)

1076, 1028  $\text{cm}^{-1}$  (C-H in-plane bending of benzene ring)

966  $\text{cm}^{-1}$  (C-H out-of-plane bending of *trans*- $\text{RCH}=\text{CHR}$ )

910  $\text{cm}^{-1}$  (C-H out-of-plane bending of  $\text{RCH}=\text{CH}_2$ )

760, 699  $\text{cm}^{-1}$  (C-H out-of-plane bending of monosubstituted benzene ring)

500  $\text{cm}^{-1}$  (Zn-O asymmetric stretching of ZnO)

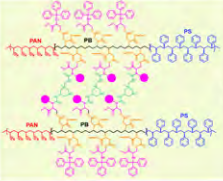
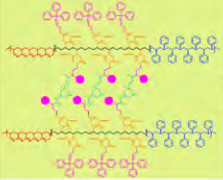
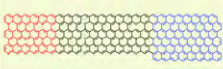


The details of *ex-situ* FTIR responses of residual solid intermediates are as follows.

i) At 50–450°C, the signals of -CH<sub>2</sub>- (2922, 2849 cm<sup>-1</sup>) in three samples gradually weaken and finally disappear at 450°C, which demonstrates dehydrogenation of the backbone structure for ABS-V and ABS. Besides, the gradually weakening until disappearing of sharp benzene ring signals (1602, 1494, 1453, 760, 699 cm<sup>-1</sup>) indicates the dehydrogenation in benzene ring-containing structures.

ii) At 450–1100°C, the emerged broad peaks between 1100–580 cm<sup>-1</sup> of ZnC-V and ZnC-A suggest the presence of possible zinc-containing inorganic compounds in residual solid intermediates (including Zn-OH libration at 715 and 901 cm<sup>-1</sup>, O-H libration from 1080 to 715 cm<sup>-1</sup>, O-H bending in 1046 and 950 cm<sup>-1</sup>, Zn-O lattice at 600 cm<sup>-1</sup>, CO<sub>3</sub> ν<sub>2</sub> to ν<sub>4</sub> at 830-700 cm<sup>-1</sup>). The signals of ZnO and possible zinc-containing inorganic compounds gradually weaken and finally disappear, which demonstrates the zinc-containing intermediates are generated from ZnO and finally decompose into volatile species. It can be inferred that a carbothermal reduction reaction occurs in this stage ( $\text{ZnO} + \text{C} \rightarrow \text{Zn} + \text{CO}$ ).<sup>7</sup> Due to the low amount of zinc-containing intermediate products generated during the carbon thermal reduction process and their rapid decomposition into volatile zinc that is carried away by protective gas, no corresponding peaks appeared in the XRD analysis.

Heating process		Pyrolysis process		
		ABS-V and ZnO (ZnC-V)	ABS and ZnO (ZnC-A)	ABS (C-A)
<b>Stage I</b> (<200°C)	<200°C	Volatilization of free water, residual DMF solvents, and unreacted monomer occurs. No chemical reactions are observed.		
<b>Stage II</b> (200-350°C)	205-320°C	Decomposition of crosslinking linkage units occurs to release CO <sub>2</sub> .	_____	_____
	232-350°C	Cyclization and dehydrogenation reaction in PAN and crosslinking linkage units begins to release olefin.	_____	_____
	290-350°C	Decomposition reaction in crosslinking linkage units starts to release benzene derivative.	_____	_____
<b>Stage III</b> (350-500°C)	355-410°C	_____	Decomposition of PB units starts to release alkanes.	_____
	370-490°C	Decomposition of PS units starts. The strongest decomposition occurs at 430-460°C when the backbone structure of PAN, PB, and PS units decompose simultaneously to release NH <sub>3</sub> , benzene derivatives, alkanes, olefins, CH <sub>4</sub> , and C <sub>2</sub> H <sub>4</sub> . The addition of ZnO promotes the decomposition of ABS-V in ZnC-V sample and suppresses the decomposition of ABS in ZnC-A sample. The backbone structures and benzene ring-containing structures of ABS-V and ABS have basically completely dehydrogenated and polycondensated into char.		
	430-490°C	Productions of some volatile products, including H <sub>2</sub> O, CO, CO <sub>2</sub> , cyano-containing compounds, are greatly inhibited by ZnO. Production of certain volatile products, including NH <sub>3</sub> , benzene derivatives, alkanes, and olefins, are partially impeded by ZnO. A little zinc-containing inorganic compounds may generate in the residual solid intermediates (the accurate composition is difficult to determine from FTIR spectra).	Interactive decomposition among PAN, PB, and PS units in pure ABS occurs to release H <sub>2</sub> O, CO, CO <sub>2</sub> , cyano-containing compounds.	
<b>Stage IV</b> (500-1100°C)	500-1100°C	Further decomposition of solid residues and elimination of heteroatoms occur to release volatile products, including CO, CO <sub>2</sub> , cyano-containing compounds, olefins, CH <sub>4</sub> , and C <sub>2</sub> H <sub>4</sub> . Oxygen-containing functional groups are basically completely eliminated at ~882°C.		
	500-1100°C	Compared to ZnC-A sample, more volatile decomposition products are involved in the reaction with ZnO to generate zinc-containing inorganic compounds that subsequently decompose to volatile zinc. ZnO is eventually exhausted at ~1000°C for ZnC-V sample and at ~1100°C for ZnC-A sample.		_____
<b>Stage V</b> (>1100°C)	>1100°C	Further carbonization and graphitization process.		

**Fig. S20.** Summary of pyrolysis processes.

Heating process		Pyrolysis process of ZnC-V		
		Main structure	Main reaction	Role of ZnO
<b>Stage I</b> (<200°C)	Volatilization → <200°C Polymer matrix (CH <sub>2</sub> N <sub>2</sub> O <sub>2</sub> )		Physical volatilization. No chemical reactions.	
<b>Stage II</b> (200-350°C)	Cyclization, dehydrogenation → 200-350°C Hydrocarbons (CH <sub>2</sub> N <sub>2</sub> O <sub>2</sub> )		Decomposition of crosslinking linkages. Cyclization and dehydrogenation of PAN and crosslinking linkage units.	
<b>Stage III</b> (350-500°C)	Dehydrogenation, polycondensation → 350-500°C Char (CN <sub>2</sub> O <sub>2</sub> )		Decomposition of PAN, PB, PS units. Dehydrogenation and polycondensation of backbone structures and benzene ring-containing structures. Production of char.	Facilitation in decomposition of ABS-V. Inhibition of volatile products. Productions of zinc-containing inorganic compounds.
<b>Stage IV</b> (500-1000°C)	Elimination of heteroatoms → 500-1000°C Char (C)		Further decomposition of solid residues. Elimination of residual heteroatoms.	Carbothermal reduction reaction.
<b>Stage V</b> (>1000°C)	Carbonization → >1000°C Porous carbon (C)		Further carbonization and graphitization process.	

**Fig. S21.** Chemical evolution during synthesis of ZnC-V.

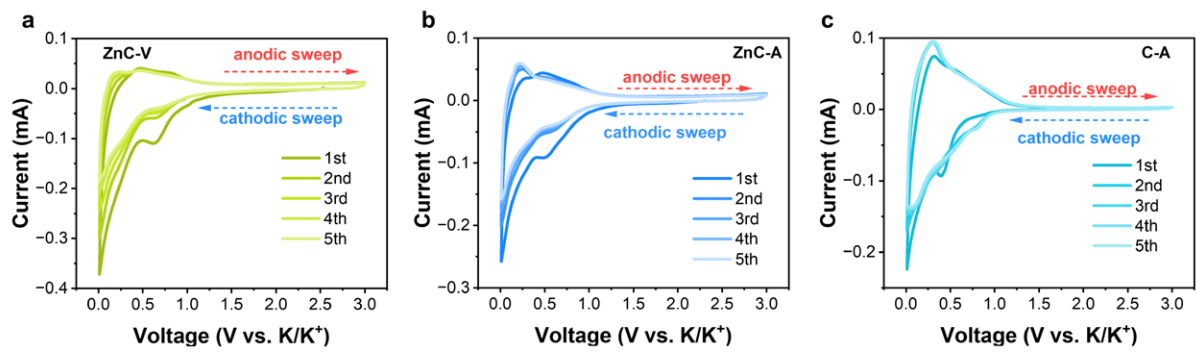


**Fig. S22.** CV curves at a scan speed of  $0.1 \text{ mV s}^{-1}$ . (a) ZnC-V. (b) ZnC-A. (c) C-A.

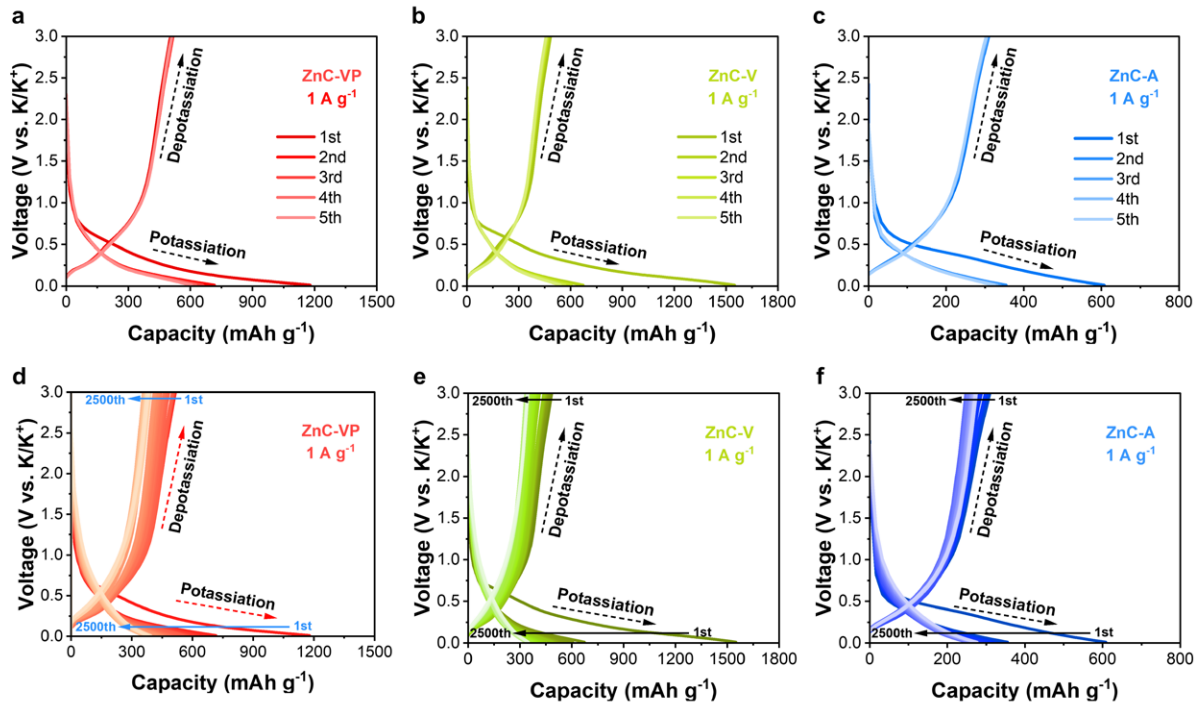


**Fig. S23.** GCD profiles at 1 A g<sup>-1</sup>. (a) ZnC-VP for the initial five cycles. (b) ZnC-V for the initial five cycles. (c) ZnC-A for the initial five cycles. (d) ZnC-VP for all cycles. (e) ZnC-V for all cycles. (f) ZnC-A for all cycles.

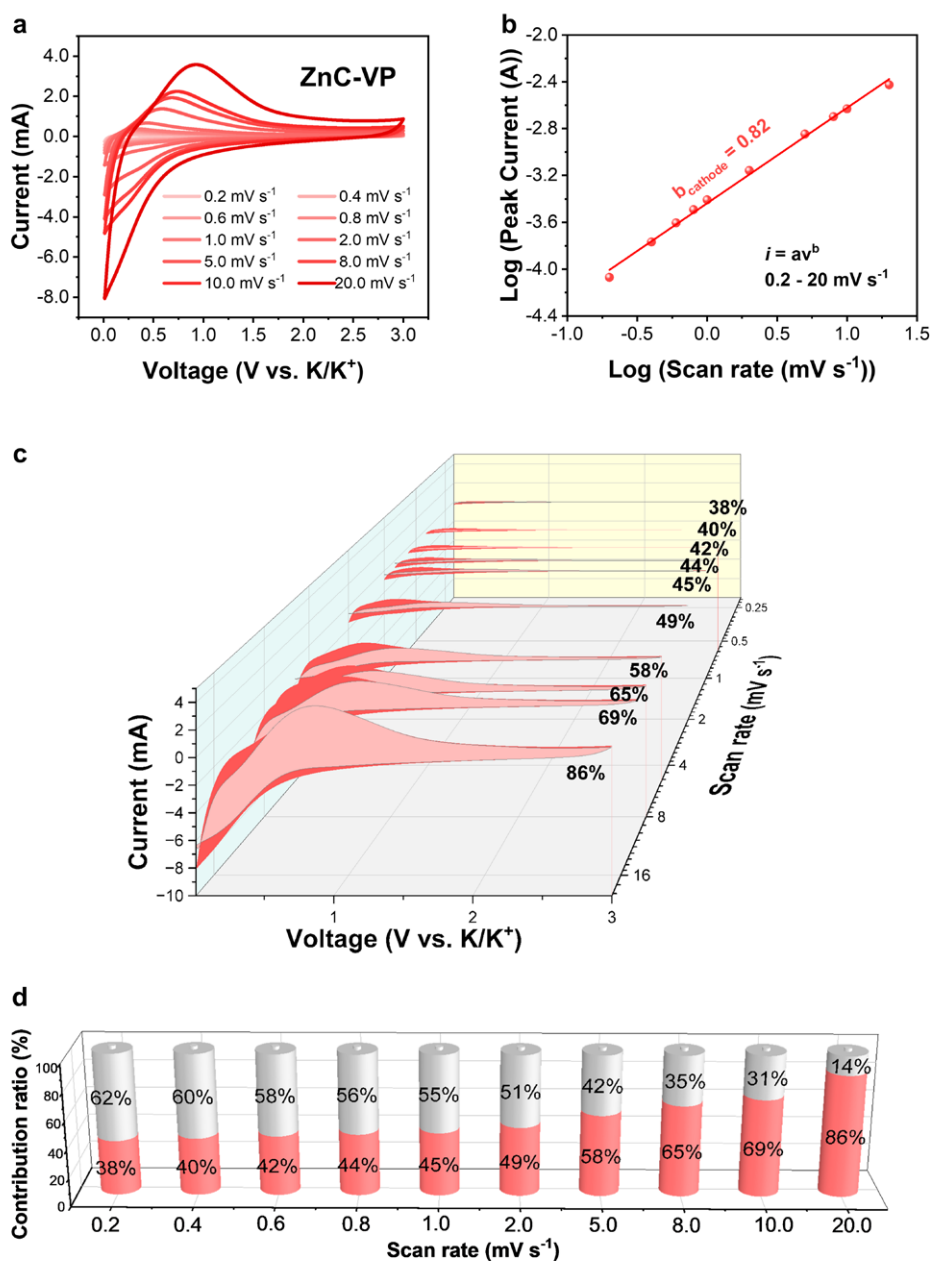


**Fig. S24.** Tests of potassium ion storage kinetics of ZnC-VP. (a) CV curves at different scan rates. (b)  $\log(i)$ - $\log(v)$  curve for calculating  $b$  value. (c) Stacked area chart of capacitive- and diffusion- controlled contributions in CV, where the enclosed area is the capacitive contribution. (d) Capacitance-dominated capacity at different scan rates.

The following equation can determine the contribution of capacitive-controlled and diffusion-controlled contributions in CV, and the value  $b$  can be obtained according to the relationship between peak current ( $i$ ) and sweep speed ( $v$ ) in formula S1:

$$i = av^b \quad (\text{S1})$$

where  $a$  and  $b$  are adjustable parameters, and  $b$  value can be determined. When  $b = 0.5$ , it is nearly considered to be a perfect diffusion-controlled process, while  $b = 1$  is considered to be a capacitive-controlled behavior.

Moreover, the contribution of capacitive and diffusion behaviors can be further analyzed by formula S2:

$$i_V = i_{\text{capacitive}} + i_{\text{diffusion}} = k_1 v + k_2 v^{1/2} \quad (\text{S2})$$

where  $i_V$  is the current value under the selected voltage  $V$ ,  $k_1 v$  represents the contribution of capacitive behavior, and  $k_2 v^{1/2}$  represents the contribution of diffusion behavior. The  $k_1$  value is obtained by fitting the relationship between  $i_V/v^{1/2}$  and  $v^{1/2}$ .

The  $b$  values of ZnC-VP, ZnC-V, ZnC-A, and C-A are calculated to be 0.82, 0.81, 0.74, and 0.61, respectively, in Fig. S24-27.



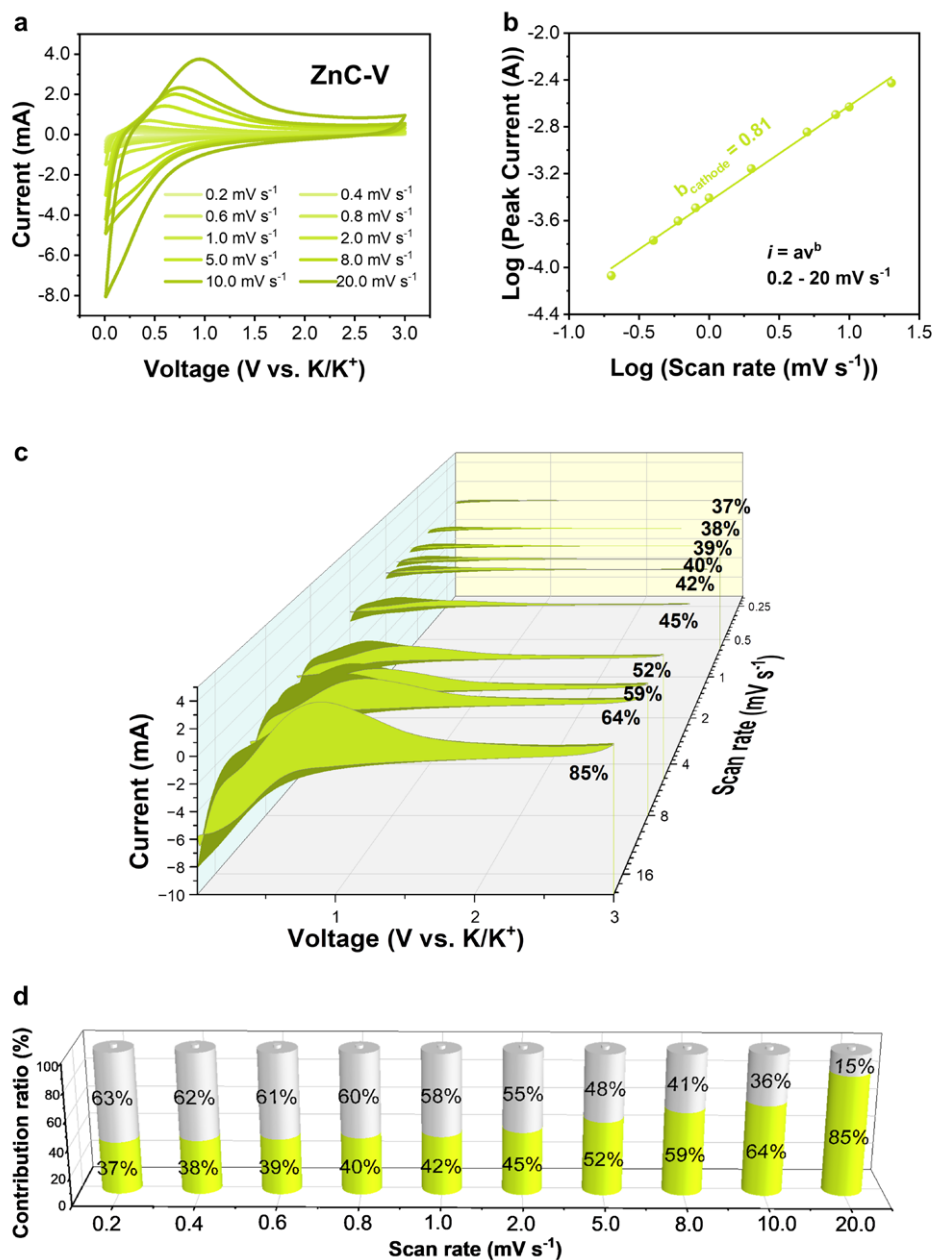


**Fig. S25.** Tests of potassium ion storage kinetics of ZnC-V. (a) CV curves at different scan rates. (b)  $\log(i)$ - $\log(v)$  curve for calculating  $b$  value. (c) Stacked area chart of capacitive- and diffusion- controlled contributions in CV, where the enclosed area is the capacitive contribution. (d) Capacitance-dominated capacity at different scan rates.

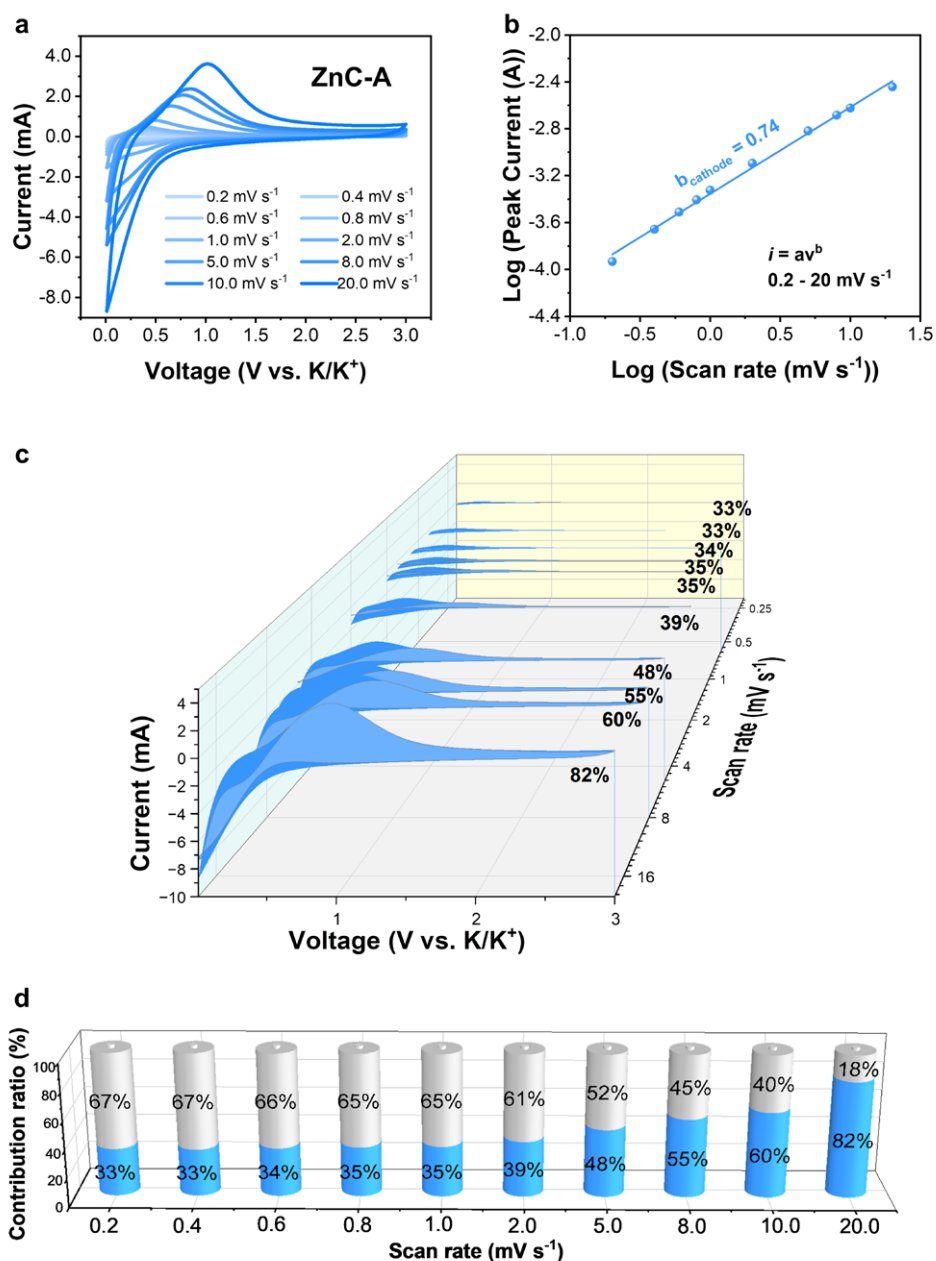


**Fig. S26.** Tests of potassium ion storage kinetics of ZnC-A. (a) CV curves at different scan rates. (b)  $\log(i)$ - $\log(v)$  curve for calculating  $b$  value. (c) Stacked area chart of capacitive- and diffusion- controlled contributions in CV, where the enclosed area is the capacitive contribution. (d) Capacitance-dominated capacity at different scan rates.

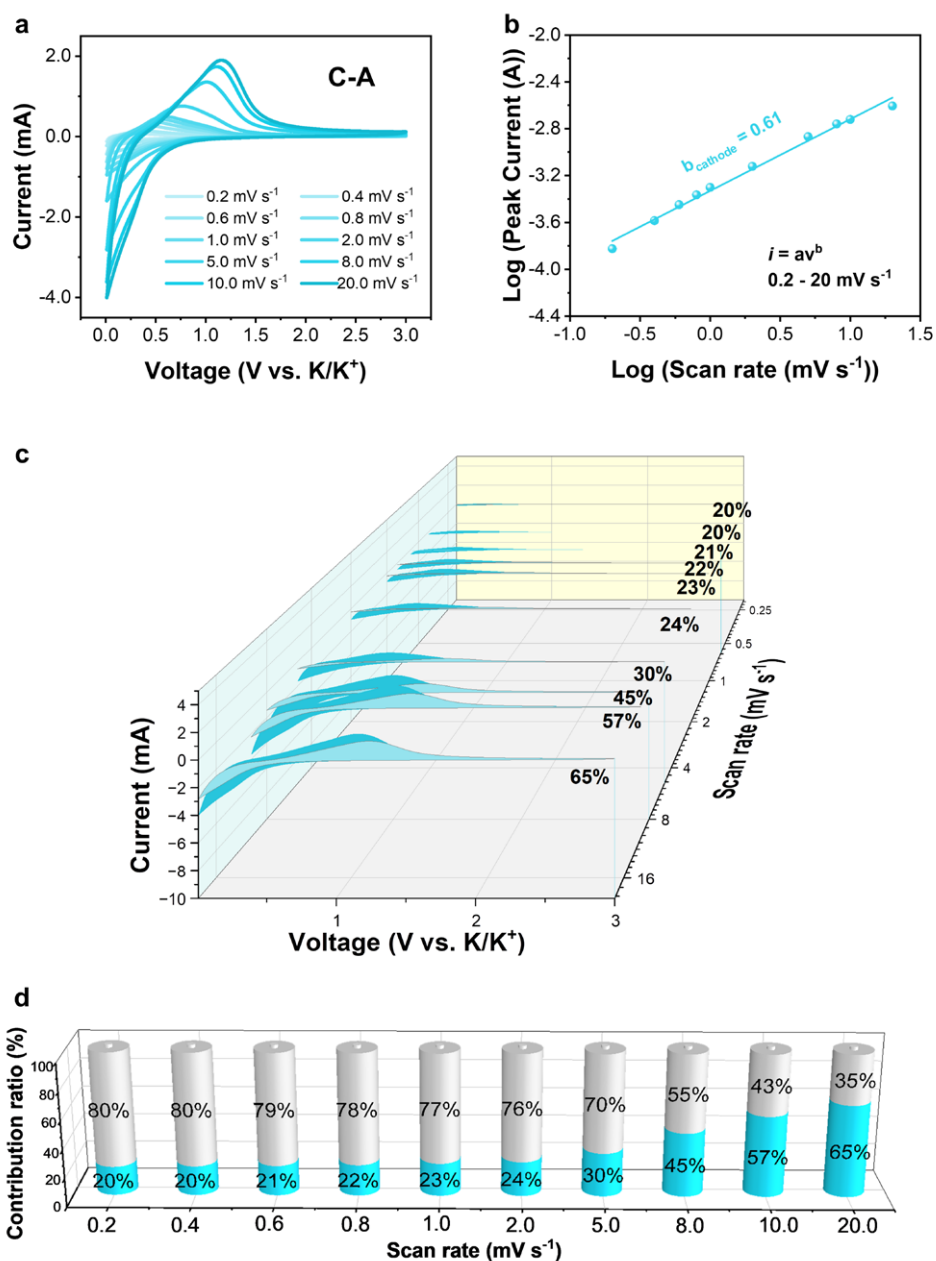


**Fig. S27.** Tests of potassium ion storage kinetics of C-A. (a) CV curves at different scan rates. (b)  $\log(i)$ - $\log(v)$  curve for calculating  $b$  value. (c) Stacked area chart of capacitive- and diffusion- controlled contributions in CV, where the enclosed area is the capacitive contribution. (d) Capacitance-dominated capacity at different scan rates.

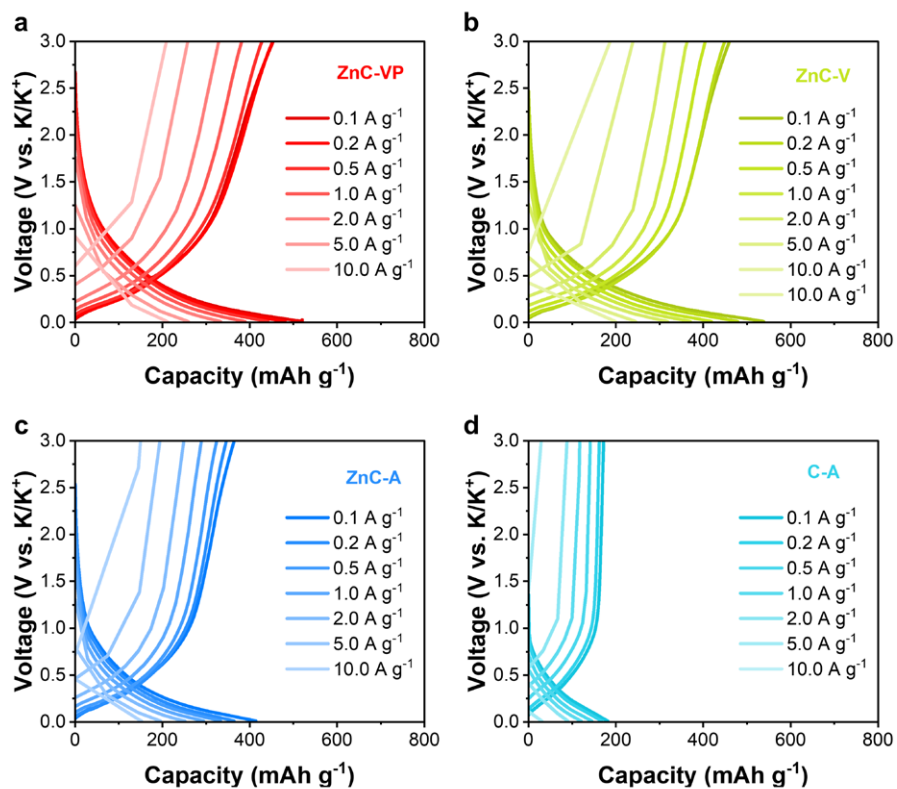


**Fig. S28.** GCD profiles at different currents. (a) ZnC-VP. (b) ZnC-V. (c) ZnC-A. (d) C-A.

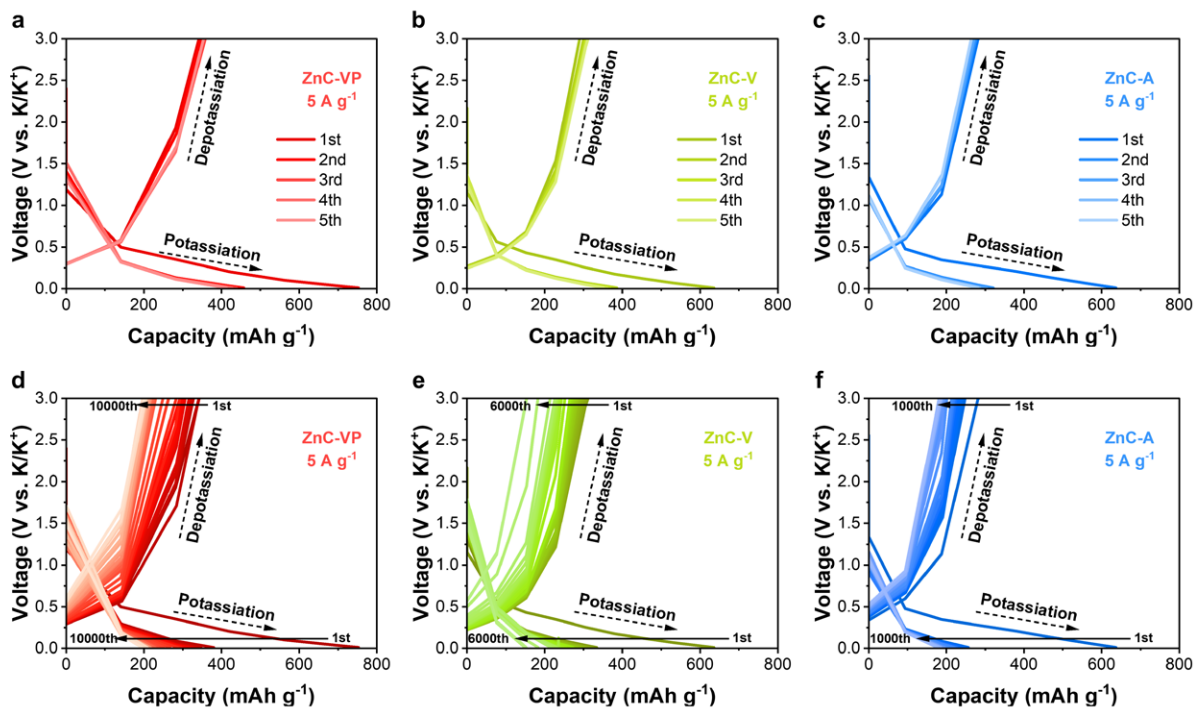


**Fig. S29.** GCD profiles at 5 A g<sup>-1</sup>. (a) ZnC-VP for the initial five cycles. (b) ZnC-V for the initial five cycles. (c) ZnC-A for the initial five cycles. (d) ZnC-VP for all cycles. (e) ZnC-V for all cycles. (f) ZnC-A for all cycles.

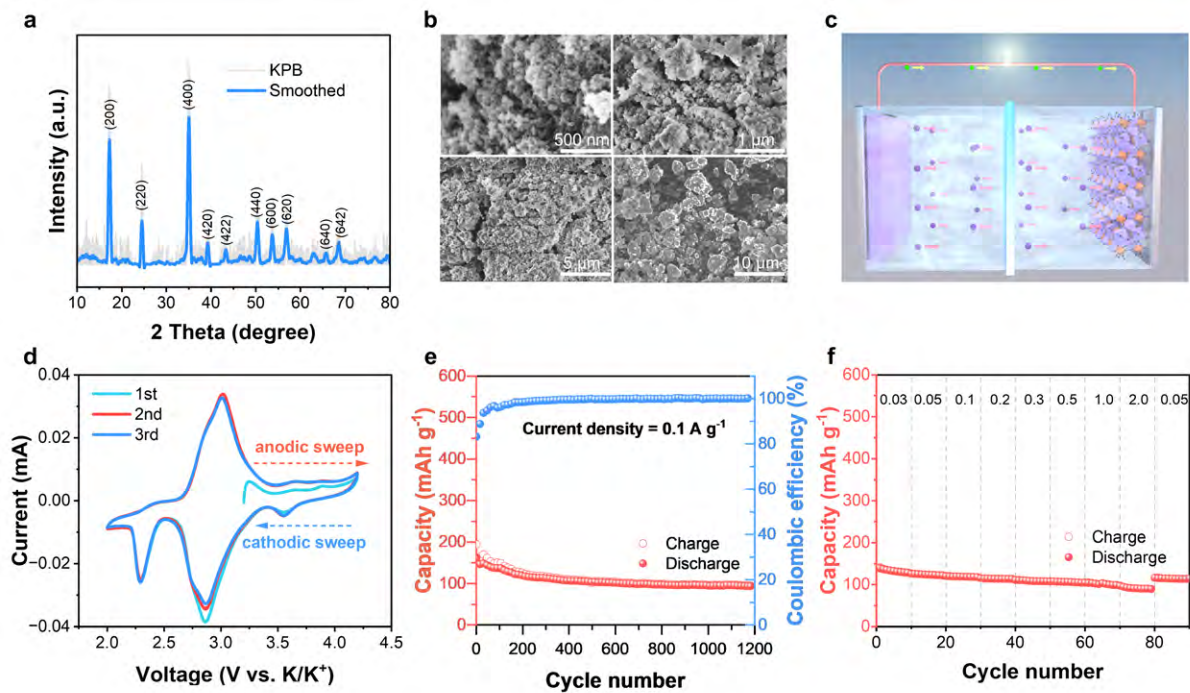


**Fig. S30.** Evaluations of Prussian Blue cathode material. (a) XRD pattern. (b) SEM image. (c) Schematic of Prussian Blue half cell. (d) CV curves at 0.1 mV s<sup>-1</sup>. (e) Cycling performance at 0.1 A g<sup>-1</sup>. (f) Capabilities at different current densities.

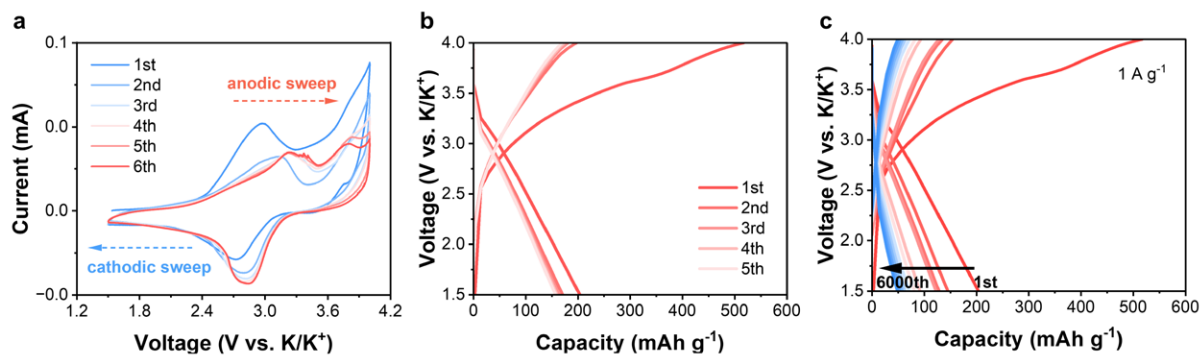


**Fig. S31.** Electrochemical behavior of ZnC-VP || Prussian Blue full cell. (a) CV curves at a scan rate of  $0.1 \text{ mV s}^{-1}$ . (b) The first five GCD curves at  $1 \text{ A g}^{-1}$ . (c) GCD curves at different cycles at  $1 \text{ A g}^{-1}$ .

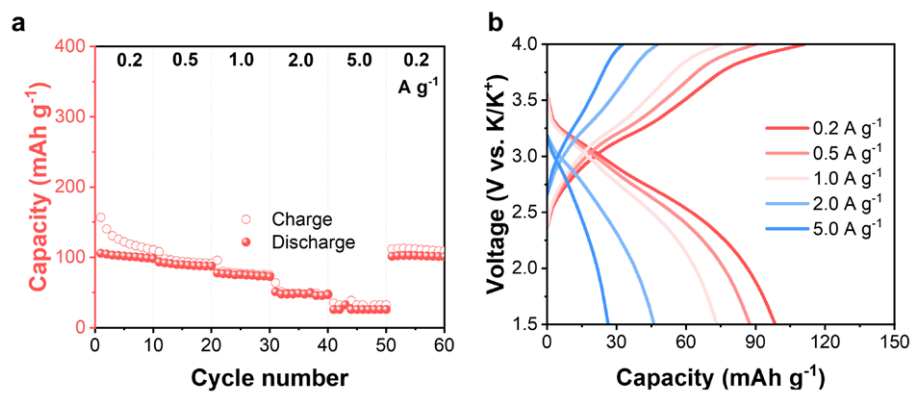


**Fig. S32.** Rate capability of ZnC-VP || Prussian Blue full cell. (a) Rate capability. (b) GCD profiles.



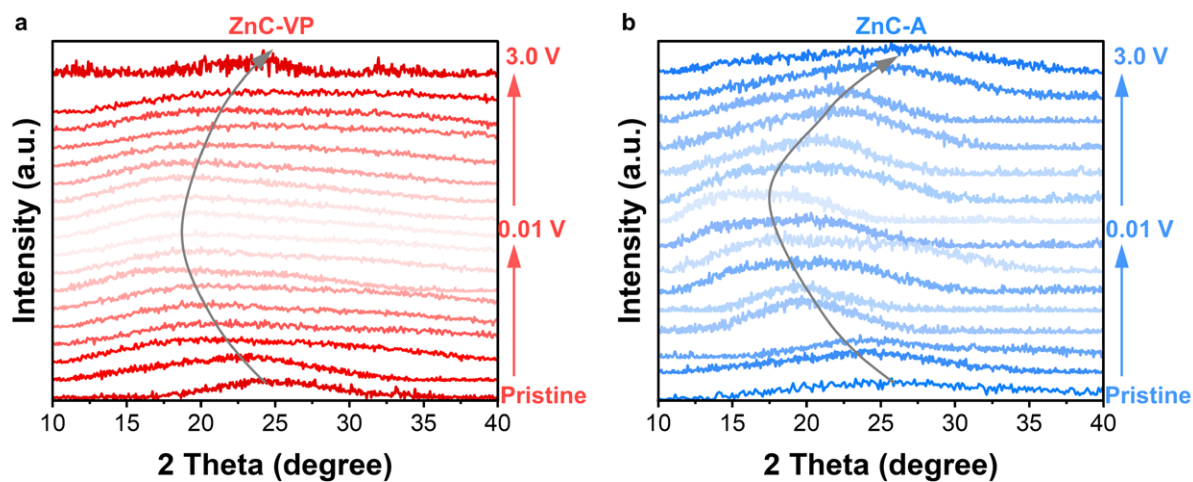


**Fig. S33.** *Ex-situ* XRD patterns at marked discharge/charge potentials. When firstly discharged to 0.01 V, the potassiation makes the graphitic interlayer spacing become larger. The (002) crystalline plane recovers after depotassiation. The potassiation expansion ratio of ZnC-VP (26.5%) is smaller than that of ZnC-A (38.2%).

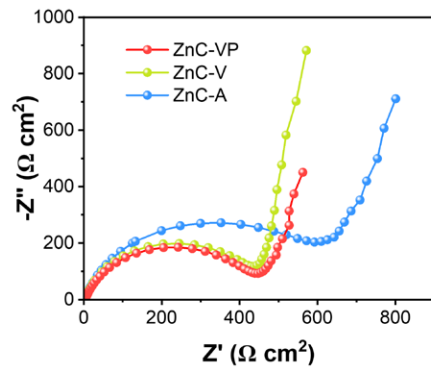


**Fig. S34.** Nyquist plots obtained with a bias of 2.0 V vs. K/K<sup>+</sup>.

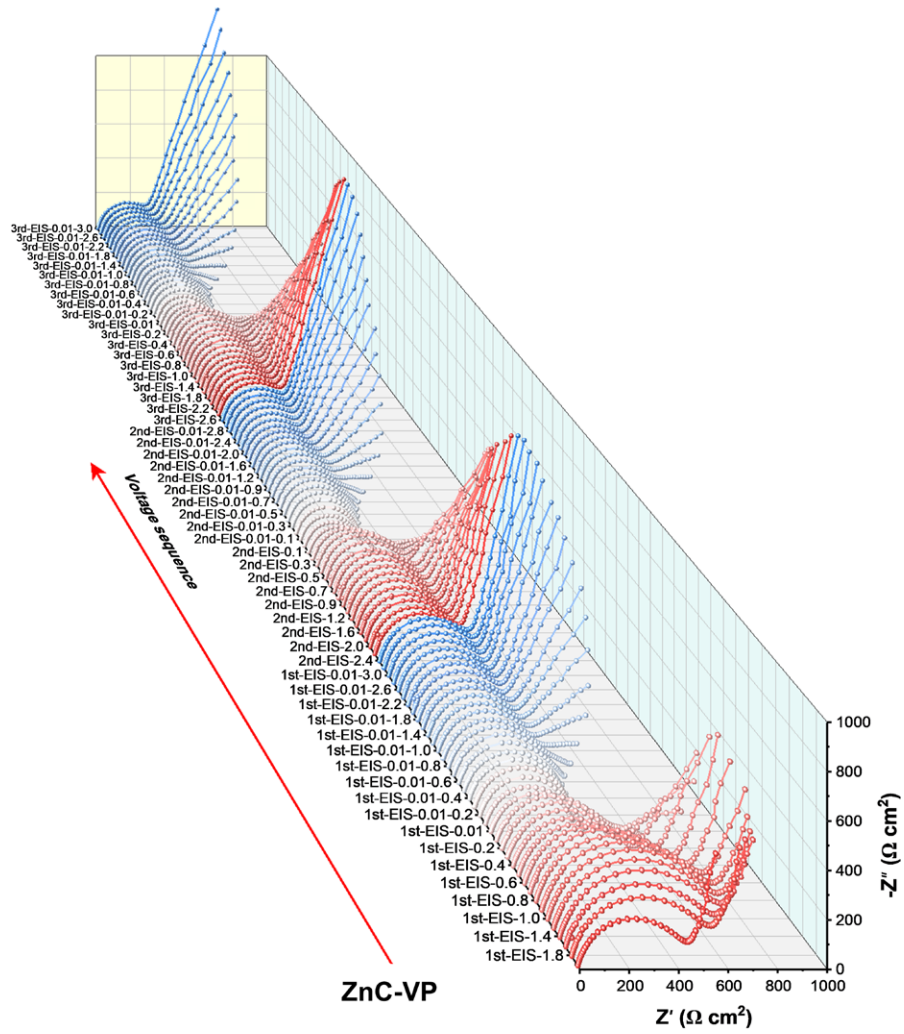


**Fig. S35.** EIS of ZnC-VP at different states during initial three cycles.

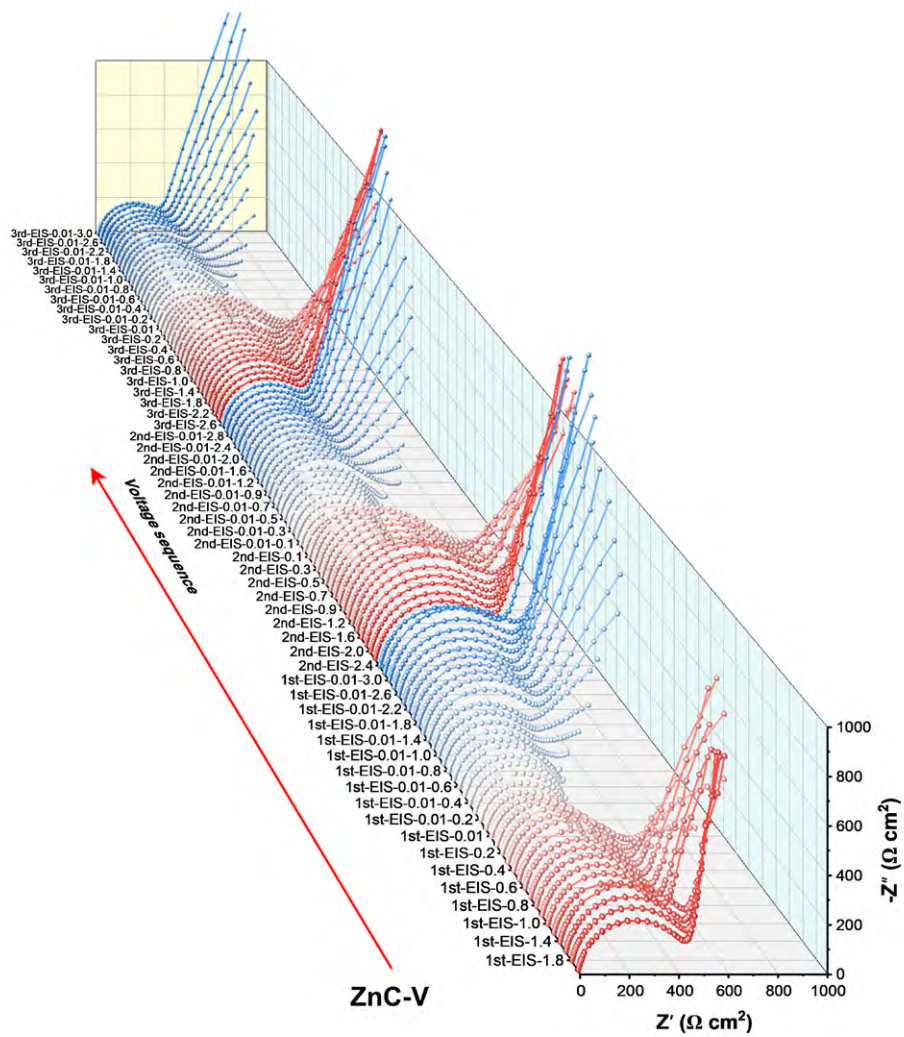


**Fig. S36.** EIS of ZnC-V at different states during initial three cycles.

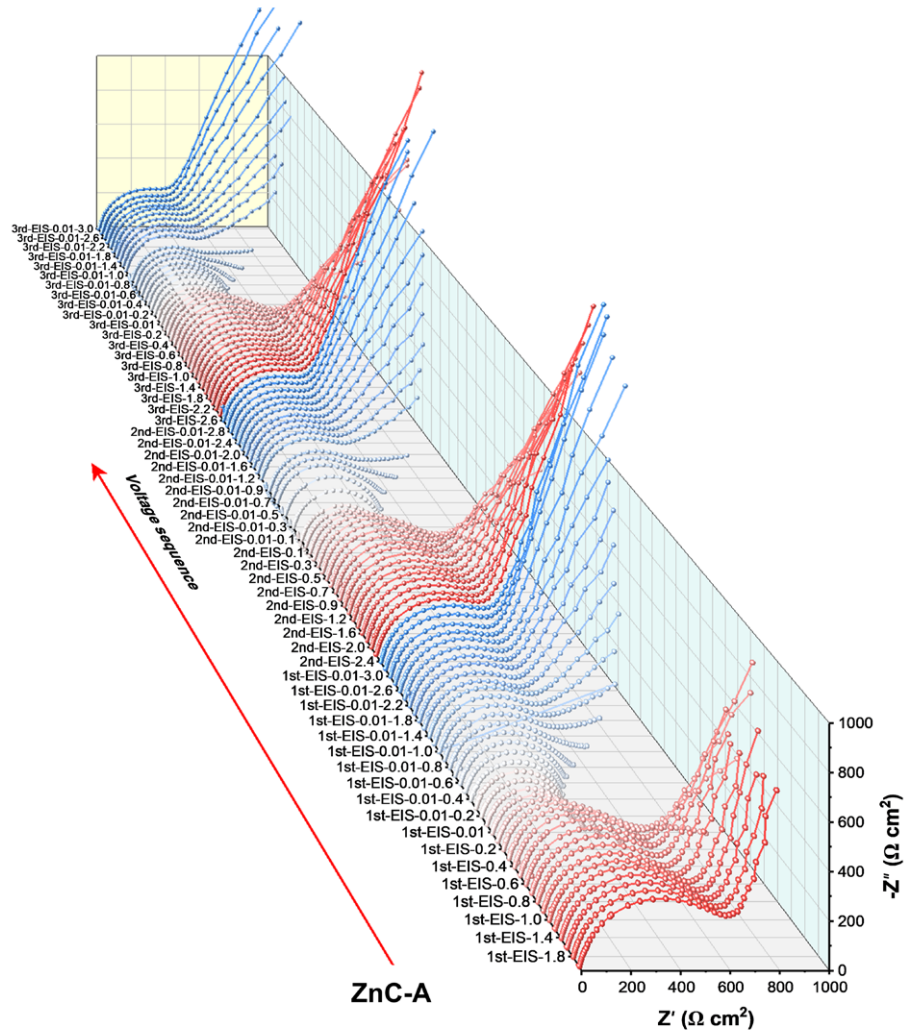
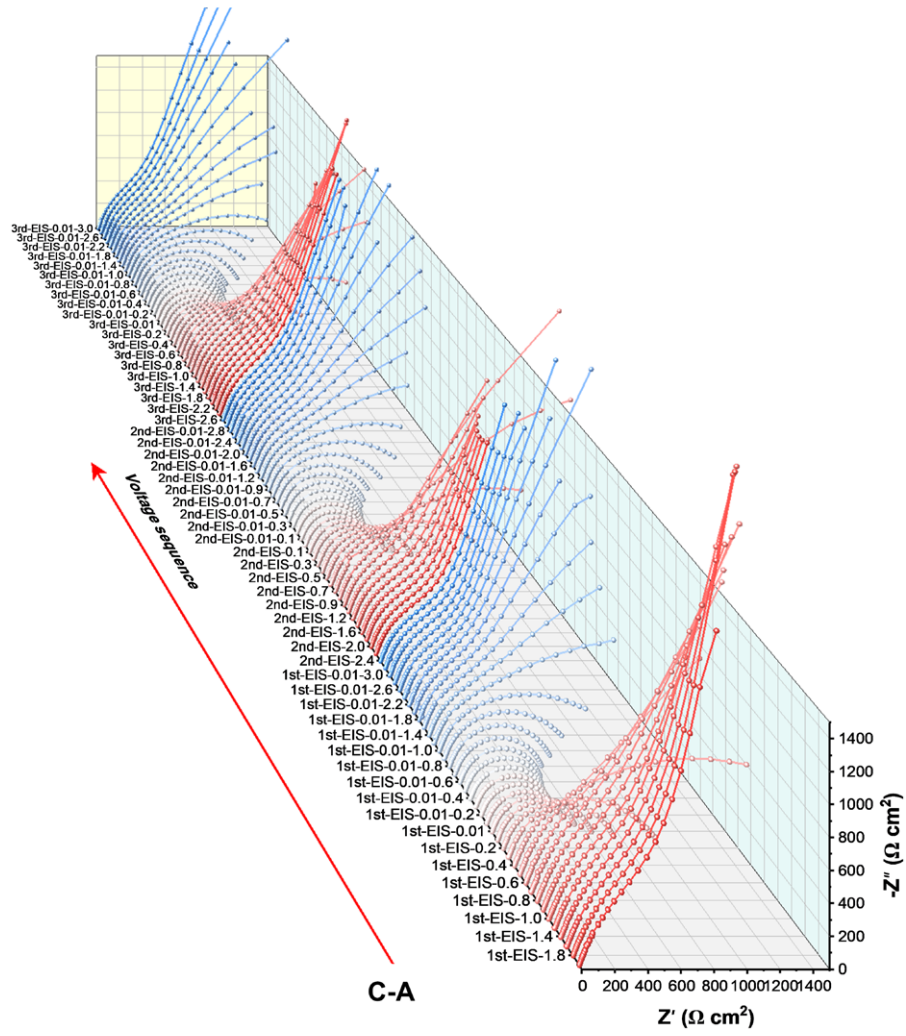
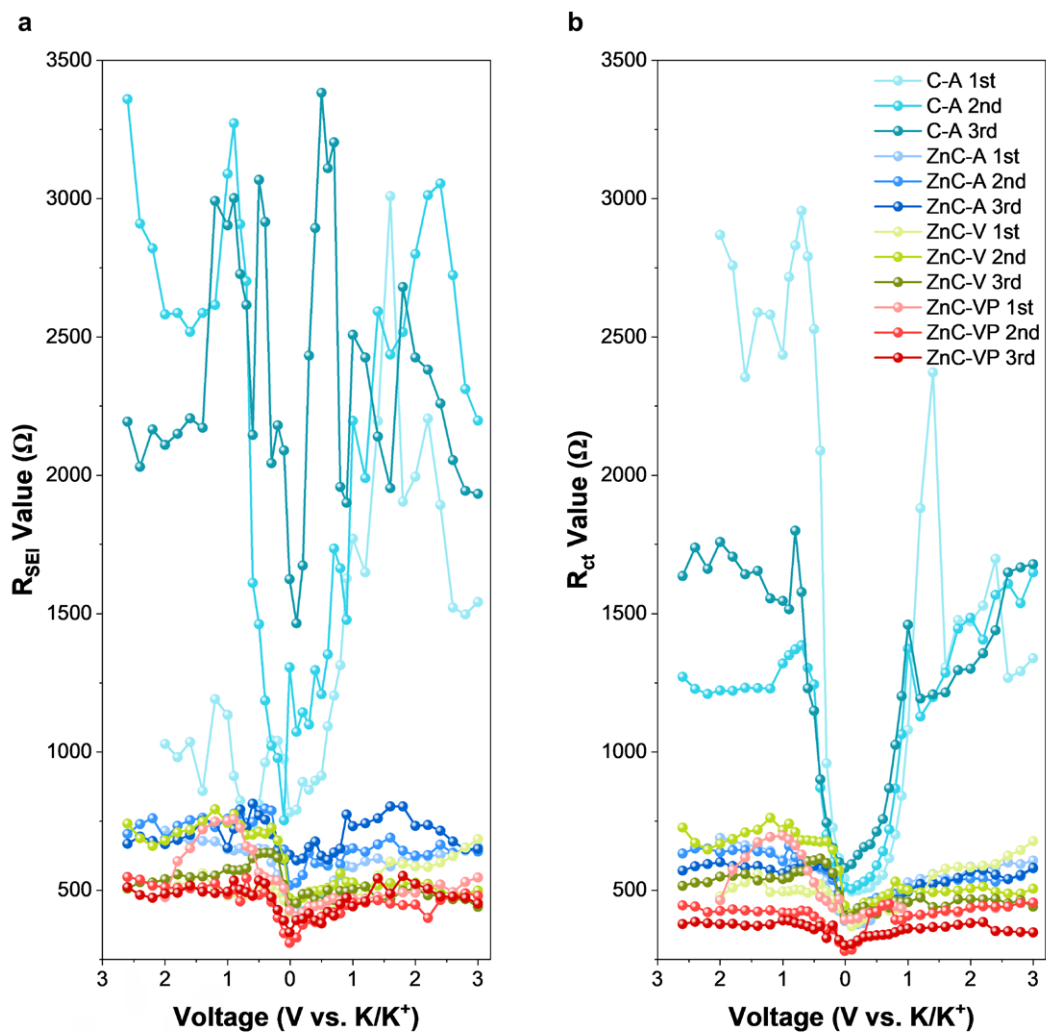


Fig. S37. EIS of ZnC-A at different states during initial three cycles.



**Fig. S38.** EIS of C-A at different states during initial three cycles.



**Fig. S39.**  $R_{SEI}$  and  $R_{ct}$  under the initial three cycles.

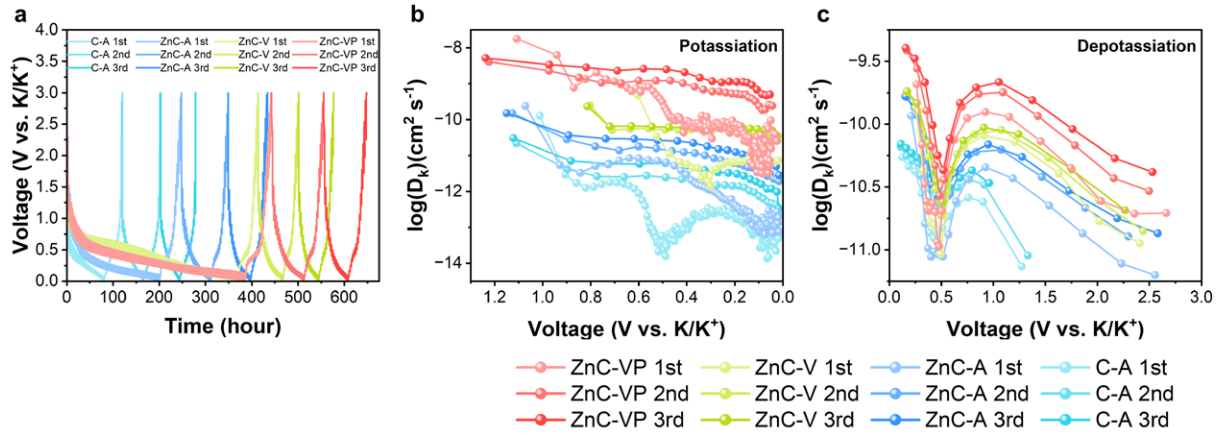


**Fig. S40.** GITT and chemical diffusion coefficients. (a) GITT profiles at the initial three cycles. (b,c) Chemical diffusion coefficients calculated under the potassiation and depotassiation processes, respectively.

The calculation formula is as follows.

$$D_k = \frac{4}{\pi\tau} \left( \frac{m_a V_m}{M_a S} \right)^2 \left( \frac{\Delta E_s}{\Delta E_t} \right)^2 \quad (\text{S3})$$

where  $\tau$  is the duration of the current pulse,  $m_a$  is the mass of the active material,  $M_a$  is the molar mass of the active material,  $S$  is the electrode-and-electrolyte contact area,  $\Delta E_s$  is the steady-state voltage change before and after the applied current pulse, and  $\Delta E_t$  is the transient voltage change caused by the current pulse.



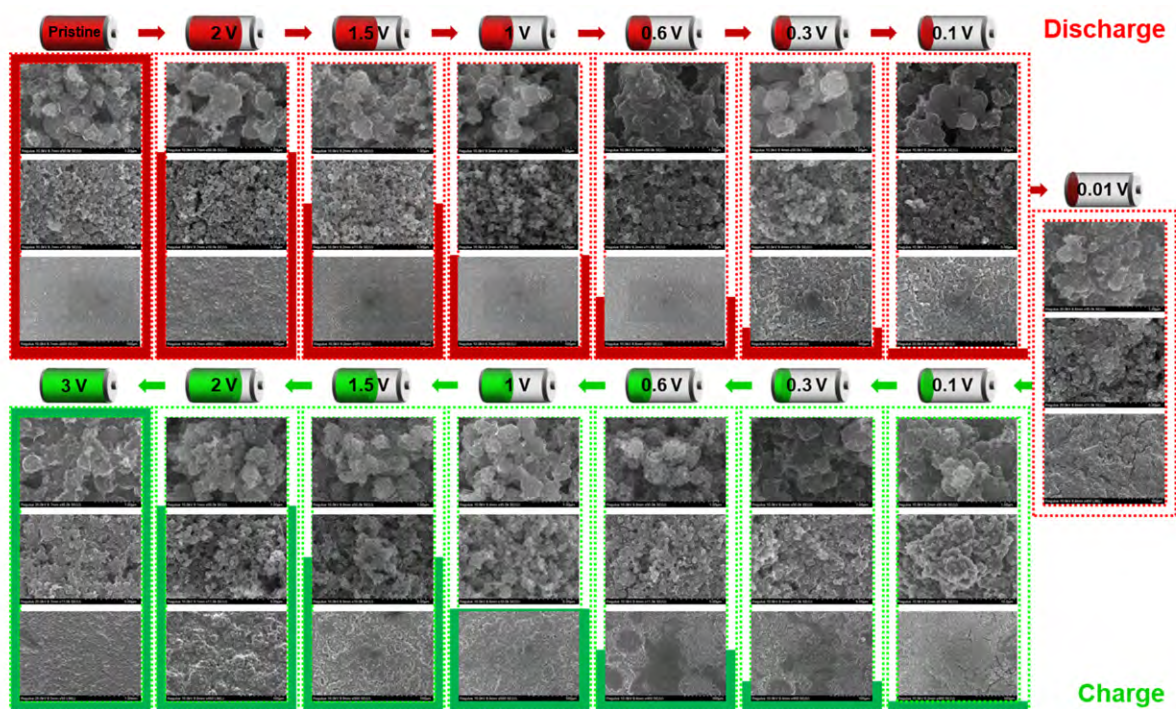


**Fig. S41.** SEM images of ZnC-VP at different discharge and charge stages.

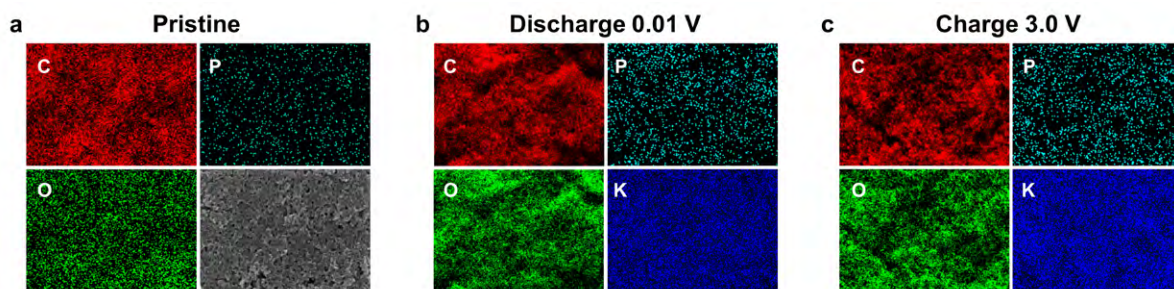


**Fig. S42.** Elemental mappings of C, P, O, and K elements of ZnC-VP. (a) Pristine state. (b) Fully discharged state. (c) Fully charged state.

**Tab. S1.** Survey of reported carbonaceous anode materials for PIBs.

Materials	Carbon sources	Additives	Rate capability	Cycling performance	Ref.
<b>ZnC-VP</b>	Recyclable ABS-V	ZnO	454 mAh g <sup>-1</sup> at 100 mA g <sup>-1</sup>	367 mAh g <sup>-1</sup> after 2500 cycles at	This work
			452 mAh g <sup>-1</sup> at 200 mA g <sup>-1</sup>	1000 mA g <sup>-1</sup>	
			428 mAh g <sup>-1</sup> at 500 mA g <sup>-1</sup>		
			381 mAh g <sup>-1</sup> at 1000 mA g <sup>-1</sup>	192 mAh g <sup>-1</sup> after 10000 cycles at	
			330 mAh g <sup>-1</sup> at 2000 mA g <sup>-1</sup>	5000 mA g <sup>-1</sup>	
			258 mAh g <sup>-1</sup> at 5000 mA g <sup>-1</sup>		
			209 mAh g <sup>-1</sup> at 10000 mA g <sup>-1</sup>		
<b>CNF</b>	Lignin and PAN		245 mAh g <sup>-1</sup> at 50 mA g <sup>-1</sup>	232 mAh g <sup>-1</sup> after 50 cycles at 100	8
			205 mAh g <sup>-1</sup> at 100 mA g <sup>-1</sup>	mA g <sup>-1</sup>	
			186 mAh g <sup>-1</sup> at 250 mA g <sup>-1</sup>		
			175 mAh g <sup>-1</sup> at 500 mA g <sup>-1</sup>		
			157 mAh g <sup>-1</sup> at 1000 mA g <sup>-1</sup>		
			143 mAh g <sup>-1</sup> at 1500 mA g <sup>-1</sup>		
<b>P-MgO</b>	Mesophase pitch	MgO	290 mAh g <sup>-1</sup> at 100 mA g <sup>-1</sup>	178 mAh g <sup>-1</sup> after 2000 cycles at	9
			250 mAh g <sup>-1</sup> at 200 mA g <sup>-1</sup>	1000 mA g <sup>-1</sup>	
			206 mAh g <sup>-1</sup> at 500 mA g <sup>-1</sup>		
			173 mAh g <sup>-1</sup> at 1000 mA g <sup>-1</sup>		
			146 mAh g <sup>-1</sup> at 2000 mA g <sup>-1</sup>		
			110 mAh g <sup>-1</sup> at 4000 mA g <sup>-1</sup>		
<b>OFGC</b>	Trisodium citrate dihydrate		456 mAh g <sup>-1</sup> at 50 mA g <sup>-1</sup>	360 mAh g <sup>-1</sup> after 1800 cycles at	10
			391 mAh g <sup>-1</sup> at 100 mA g <sup>-1</sup>	100 mA g <sup>-1</sup>	
			355 mAh g <sup>-1</sup> at 200 mA g <sup>-1</sup>		
			305 mAh g <sup>-1</sup> at 500 mA g <sup>-1</sup>	230 mAh g <sup>-1</sup> after 10000 cycles at	
			260 mAh g <sup>-1</sup> at 1000 mA g <sup>-1</sup>	3000 mA g <sup>-1</sup>	
			212 mAh g <sup>-1</sup> at 2000 mA g <sup>-1</sup>		
			177 mAh g <sup>-1</sup> at 3000 mA g <sup>-1</sup>		
134 mAh g <sup>-1</sup> at 5000 mA g <sup>-1</sup>					
<b>3D-NTC</b>	Pyromellitic acid, Melamine		518 mAh g <sup>-1</sup> at 50 mA g <sup>-1</sup>	247 mAh g <sup>-1</sup> after 500 cycles at	11
			436 mAh g <sup>-1</sup> at 100 mA g <sup>-1</sup>	1000 mA g <sup>-1</sup>	
			378 mAh g <sup>-1</sup> at 200 mA g <sup>-1</sup>		
			313 mAh g <sup>-1</sup> at 500 mA g <sup>-1</sup>		
			265 mAh g <sup>-1</sup> at 1000 mA g <sup>-1</sup>		
			212 mAh g <sup>-1</sup> at 2000 mA g <sup>-1</sup>		
			119 mAh g <sup>-1</sup> at 5000 mA g <sup>-1</sup>		
<b>NHC<sub>2</sub></b>	PAN	ZnO	278 mAh g <sup>-1</sup> at 50 mA g <sup>-1</sup>	161.3 mAh g <sup>-1</sup> after 1600 cycles at	12
			266 mAh g <sup>-1</sup> at 100 mA g <sup>-1</sup>	1000 mA g <sup>-1</sup>	
			261 mAh g <sup>-1</sup> at 200 mA g <sup>-1</sup>		
			243 mAh g <sup>-1</sup> at 500 mA g <sup>-1</sup>		
			224 mAh g <sup>-1</sup> at 1000 mA g <sup>-1</sup>		
			205 mAh g <sup>-1</sup> at 2000 mA g <sup>-1</sup>		
<b>CMS</b>	Graphitic C <sub>3</sub> N <sub>4</sub>	Zn	328 mAh g <sup>-1</sup> at 100 mA g <sup>-1</sup>	300mAh g <sup>-1</sup> after 1000 cycles at 100	13
			278 mAh g <sup>-1</sup> at 200 mA g <sup>-1</sup>	mA g <sup>-1</sup>	

			225 mAh g <sup>-1</sup> at 500 mA g <sup>-1</sup> 180 mAh g <sup>-1</sup> at 1000 mA g <sup>-1</sup> 150 mAh g <sup>-1</sup> at 2000 mA g <sup>-1</sup> 125 mAh g <sup>-1</sup> at 3000 mA g <sup>-1</sup>	136 mAh g <sup>-1</sup> after 10000 cycles at 2000 mA g <sup>-1</sup>	
<b>GNC</b>	EDTA	NaCl	350 mAh g <sup>-1</sup> at 50 mA g <sup>-1</sup> 270 mAh g <sup>-1</sup> at 100 mA g <sup>-1</sup> 220 mAh g <sup>-1</sup> at 200 mA g <sup>-1</sup> 180 mAh g <sup>-1</sup> at 500 mA g <sup>-1</sup> 150 mAh g <sup>-1</sup> at 1000 mA g <sup>-1</sup> 115 mAh g <sup>-1</sup> at 2000 mA g <sup>-1</sup> 50 mAh g <sup>-1</sup> at 5000 mA g <sup>-1</sup>	189 mAh g <sup>-1</sup> after 200 cycles at 200 mA g <sup>-1</sup>	14
<b>STGA</b>	rGO	S	250 mAh g <sup>-1</sup> at 100 mA g <sup>-1</sup> 200 mAh g <sup>-1</sup> at 200 mA g <sup>-1</sup> 130 mAh g <sup>-1</sup> at 500 mA g <sup>-1</sup> 110 mAh g <sup>-1</sup> at 1000 mA g <sup>-1</sup> 50 mAh g <sup>-1</sup> at 2000 mA g <sup>-1</sup>	199 mAh g <sup>-1</sup> after 500 cycles at 100 mA g <sup>-1</sup>	15
<b>SiC-CDC</b>	SiC		400 mAh g <sup>-1</sup> at 100 mA g <sup>-1</sup> 300 mAh g <sup>-1</sup> at 200 mA g <sup>-1</sup> 250 mAh g <sup>-1</sup> at 500 mA g <sup>-1</sup> 200 mAh g <sup>-1</sup> at 1000 mA g <sup>-1</sup>	285 mAh g <sup>-1</sup> after 200 cycles at 100 mA g <sup>-1</sup> 193 mAh g <sup>-1</sup> after 1000 cycles at 1000 mA g <sup>-1</sup>	16
<b>NSG</b>	Pyridine, Thiophene	MgO	192 mAh g <sup>-1</sup> at 1000 mA g <sup>-1</sup> 155 mAh g <sup>-1</sup> at 2000 mA g <sup>-1</sup> 122 mAh g <sup>-1</sup> at 5000 mA g <sup>-1</sup> 97 mAh g <sup>-1</sup> at 10000 mA g <sup>-1</sup> 91 mAh g <sup>-1</sup> at 20000 mA g <sup>-1</sup>	220 mAh g <sup>-1</sup> after 1200 cycles at 500 mA g <sup>-1</sup> 100 mAh g <sup>-1</sup> after 5000 cycles at 5000 mA g <sup>-1</sup>	17
<b>WPCS</b>	Methyl cellulose	NaHCO <sub>3</sub>	463 mAh g <sup>-1</sup> at 50 mA g <sup>-1</sup> 350 mAh g <sup>-1</sup> at 100 mA g <sup>-1</sup> 304 mAh g <sup>-1</sup> at 200 mA g <sup>-1</sup> 280 mAh g <sup>-1</sup> at 500 mA g <sup>-1</sup> 250 mAh g <sup>-1</sup> at 1000 mA g <sup>-1</sup> 223 mAh g <sup>-1</sup> at 2000 mA g <sup>-1</sup> 200 mAh g <sup>-1</sup> at 5000 mA g <sup>-1</sup>	153 mAh g <sup>-1</sup> after 5000 cycles at 2000 mA g <sup>-1</sup> 89 mAh g <sup>-1</sup> after 4000 cycles at 5000 mA g <sup>-1</sup> 53 mAh g <sup>-1</sup> after 4000 cycles at 10000 mA g <sup>-1</sup>	18
<b>N-ALC</b>	Uric acid		336 mAh g <sup>-1</sup> at 100 mA g <sup>-1</sup> 229 mAh g <sup>-1</sup> at 500 mA g <sup>-1</sup> 274 mAh g <sup>-1</sup> at 1000 mA g <sup>-1</sup>	180 mAh g <sup>-1</sup> after 2300 cycles at 1000 mA g <sup>-1</sup>	19
<b>BCCs</b>	Melamine	Co	302 mAh g <sup>-1</sup> at 100 mA g <sup>-1</sup> 248 mAh g <sup>-1</sup> at 500 mA g <sup>-1</sup> 160 mAh g <sup>-1</sup> at 1000 mA g <sup>-1</sup>	226 mAh g <sup>-1</sup> after 2100 cycles at 100 mA g <sup>-1</sup>	20
<b>FNCS</b>	PU and PTFE		610 mAh g <sup>-1</sup> at 100 mA g <sup>-1</sup> 395 mAh g <sup>-1</sup> at 500 mA g <sup>-1</sup> 324 mAh g <sup>-1</sup> at 1000 mA g <sup>-1</sup> 131 mAh g <sup>-1</sup> at 10000 mA g <sup>-1</sup>	131 mAh g <sup>-1</sup> after 4000 cycles at 5000 mA g <sup>-1</sup>	21
<b>P/O-PCS</b>	C <sub>2</sub> H <sub>2</sub>	MnCO <sub>3</sub>	281 mAh g <sup>-1</sup> at 500 mA g <sup>-1</sup> 258 mAh g <sup>-1</sup> at 1000 mA g <sup>-1</sup> 195 mAh g <sup>-1</sup> at 10000 mA g <sup>-1</sup>	154 mAh g <sup>-1</sup> after 2500 cycles at 1000 mA g <sup>-1</sup>	22

## Supporting References

1. M. Day, J. D. Cooney, C. Touchette-Barrette and S. E. Sheehan, *J. Anal. Appl. Pyrol.*, 1999, **52**, 199–224.
2. M. Brebu, M. A. Uddin, A. Muto, Y. Sakata and C. Vasile, *Energy & Fuels*, 2000, **14**, 920–928.
3. M. Brebu, M. A. Uddin, A. Muto, Y. Sakata and C. Vasile, *J. Anal. Appl. Pyrol.*, 2002, **63**, 43–57.
4. W. J. Hall and P. T. Williams, *Energy & Fuels*, 2006, **20**, 1536–1549.
5. J. M. Encinar and J. F. González, *Fuel Process. Technol.*, 2008, **89**, 678–686.
6. S. H. Jung, S. J. Kim and J. S. Kim, *Fuel Processing Technology*, 2013, **116**, 123–129.
7. H. K. Chen, *Scand. J. Metal.*, 2008, **30**, 292–296.
8. Z. L. Yu, Q. Liu, C. S. Chen, Y. Zhu and B. Zhang, *J. Power Sources*, 2022, **557**, 232592.
9. H. Tan, X. Du, R. Zhou, Z. Hou and B. Zhang, *Carbon*, 2021, **176**, 383–389.
10. N. Cheng, W. Zhou, J. Liu, Z. Liu and B. Lu, *Nano-Micro Lett.*, 2022, **14**, 146.
11. W. L. Zhang, J. Yin, M. L. Sun, W. X. Wang, C. L. Chen, M. Altunkaya, A. Emwas, Y. Han, U. Schwingenschlögl and H. N. Alshareef, *Adv. Mater.*, 2020, **32**, 2000732.
12. W. Yang, J. Zhou, S. Wang, W. Zhang, Z. Wang, F. Lv, K. Wang, Q. Sun and S. Guo, *Energ. Environ. Sci.*, 2019, **12**, 1605–1612.
13. J. Ge, B. Wang, J. Zhou, S. Liang, A. M. Rao and B. Lu, *ACS Mater. Lett.*, 2020, **2**, 853–860.
14. W. L. Zhang, J. Ming, W. L. Zhao, X. C. Dong, M. N. Hedhili, P. M. F. J. Costa and H. N. Alshareef, *Adv. Funct. Mater.*, 2019, **29**, 1903641.
15. J. W. Han, C. Zhang, D. B. Kong, X. Z. He, J. Xiao, F. Q. Chen, Y. Tao, Y. Wan and Q. H. Yang, *Nano Energy*, 2020, **72**, 104729.
16. J. Wu, X. X. Zhang, Z. Li, C. F. Yang, W. D. Zhong, W. L. Li, C. Z. Zhang, N. J. Yang, Q. Zhang and X. K. Li, *Adv. Funct. Mater.*, 2020, **30**, 2004348.
17. C. Lu, Z. Sun, L. Yu, X. Lian, Y. Yi, J. Li, Z. Liu, S. X. Dou and J. Y. Sun, *Adv. Energy Mater.*, 2020, **10**, 2001161.
18. Y. Cui, W. Liu, X. Wang, J. Li, Y. Zhang, Y. Du, S. Liu, H. Wang, W. Feng and M. Chen, *ACS Nano*, 2019, **13**, 11582–11592.
19. W. Zhang, M. Sun, J. Yin, K. Lu, U. Schwingenschlögl, X. Qiu and H. N. Alshareef, *Adv. Energy Mater.*, 2021, **11**, 2101928.
20. H. Ding, J. Zhou, A. M. Rao and B. Lu, *Nat. Sci. Rev.*, 2020, **8**, nwaa276.
21. Y. Jiang, Y. Yang, R. Xu, X. L. Chen, H. J. Huang, P. C. Shi, Y. Yao, H. Yang, D. J. Li, X. F. Zhou, Q. W. Chen, Y. Z. Feng, X. H. Rui and Y. Yu, *ACS Nano*, 2021, **15**, 10217–10227.
22. S. Zhao, K. Yan, J. Liang, Q. Yuan, J. Zhang, B. Sun, P. Munroe and G. Wang, *Advanced Funct. Mater.*, 2021, **31**, 2102060.